CHALMERS
UNIVERSITY OF TECHNOLOGY

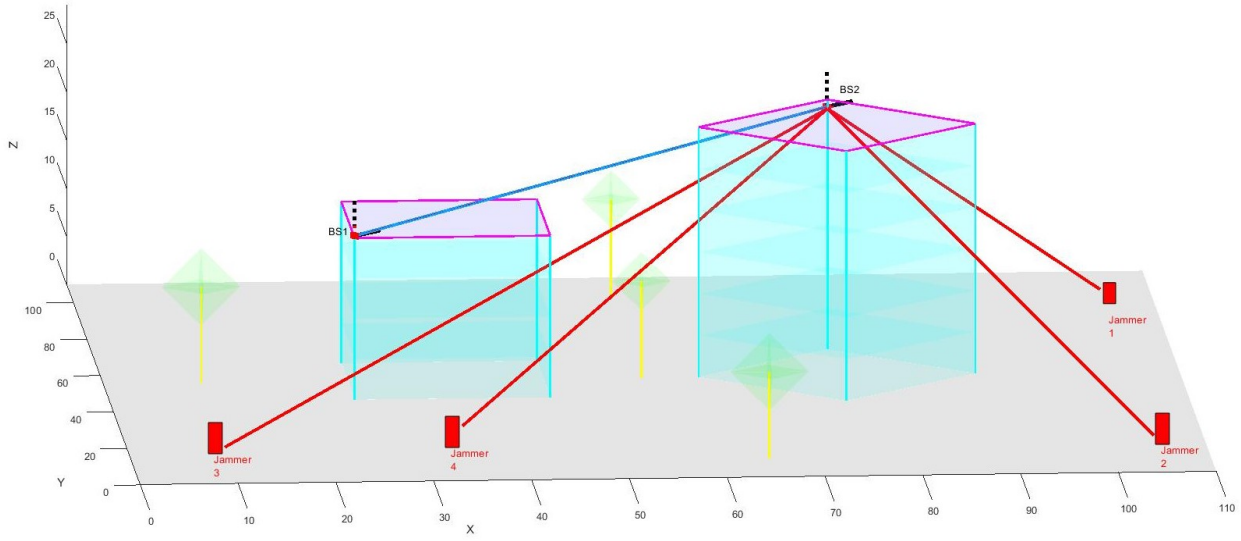

Adaptive Interference Suppression Algorithm for Analog Beamforming

Master's thesis in Communication Engineering

Abdullah Yousif Asaad

Department of Electrical Engineering
CHALMERS UNIVERSITY OF TECHNOLOGY
Gothenburg, Sweden 2020

Master's thesis 2020

Adaptive Interference Suppression Algorithm for Analog Beamforming

Abdullah Yousif Asaad

CHALMERS
UNIVERSITY OF TECHNOLOGY

Department of Electrical Engineering
Chalmers University of Technology
Gothenburg, Sweden 2020

Adaptive Interference Suppression Algorithm for Analog Beamforming
Abdullah Yousif Asaad

Supervisor: Mats Alexanderson, Huawei Technologies Sweden AB
Supervisor: Yasaman Ettefagh, Department of Electrical Engineering
Examiner: Tommy Svensson, Department of Electrical Engineering

Master's Thesis 2020
Department of Electrical Engineering
Chalmers University of Technology
SE-412 96 Gothenburg
Telephone +46 31 772 1000

Cover: Interference scenario constructed in Matlab showing multiple jamming signals interfering with a desired signal.

Typeset in LaTeX
Printed by [Name of printing company]
Gothenburg, Sweden 2020

Adaptive Interference Suppression Algorithm for Analog Beamforming
Abdullah Yousif Asaad
Department of Electrical Engineering
Chalmers University of Technology

Abstract

Intergrated Access and Backhaul (IAB) in 5G makes deployment of base stations cheaper, but this is at the expense of more interference caused by undesired signals. Moreover, if the undesired signal is strong enough or is wideband, the receiver fails to establish any sort of reliable communication with the transmitter and thus, suppressing interference becomes a crucial requirement for IAB. In this thesis, interference suppression is achieved by implementing the Applebaum algorithm in an IAB scenario for mm-wave frequency bands. The scenario includes a link budget that tracks transmission from one base station to another with no jamming signals initially present and then moves on to record what happens when single and multiple jammers are introduced. It is assumed that the Angle of Arrival (AoA) for the jammers are known and that the algorithm uses the covariance matrix of the noise at antenna elements to find the optimal weights required for each scenario. In the case of no jammers, the noise component at different antenna elements are uncorrelated so, the covariance matix of the noise is a diagonal matrix which ensures maximum Signal to Noise Ratio (SNR) of the antenna array. However, when single and multiple jammers are introduced, the noise component of different antenna elements are correlated and the covariance matrix of the noise is a symmetrical matrix, which reduces system performance by causing a decrease in the total SNR of the antenna array. The optimal weights produced by the algorithm improves system performance by producing deep nulls at the location of the jammer. For multiple jammers, the algorithm is more limited and as a result, system performance is compromised.

Keywords: IAB, interference suppression, angle of arrival, covariance matrix, multiple jammers, radiation pattern, nulls, system performance.

Acknowledgements

I would like to thank Yasaman Ettefagh for her continual efforts in helping and guiding me; the report could not have been written without her. Her attention to detail, patience and sheer competence as an advisor was a major driving force behind this thesis. I would also like to thank Mats Alexanderson for his help. His astute technical prowess was without doubt a major influence in this thesis. His capability of remaining calm when confronted with a problem helped me fortify my own mind in moments of uncertainty. Finally, I would like to thank my examiner Tommy Svensson, who's contacts with Huawei technologies made this thesis possible. He helped guide me with both the planning and final report and his willingness to be of sincere help in any technical or practical matters whenever called for was much appreciated.

Abdullah Yousif Asaad, Gothenburg, January 2020

Contents

List of Figures

List of Tables

1
Introduction

Mobile networks in today's world use frequencies below 6 GHz. The industry, however, suggests that mobile networks could find use in many more applications by using millimeter-Wave (mm-Wave) frequencies, such as 28 GHz [1]. The proper utilization of higher frequency bands for mobile access would allow for more bandwidth. More bandwidth could dismiss the need for fiber-based backhaul, by enabling integrated access and backhaul to share the same frequency band. As a result, this would save costs and time needed to deploy fiber to many small cell base stations [2]. With integrated access and backhaul (IAB) techniques, there would be more flexibility in spectrum allocation; but, this would be at the expense of more interference [3] and thus, a greater need for interference rejection methods. Also, higher frequencies cause greater path loss, this, in turn, limits the minimum transmission power from transmitters. Fortunately, the constraints that come with deploying high frequencies and IAB can be mitigated by using adaptive antenna phase arrays. Through proper beamforming, adaptive antenna phase arrays can cancel interfering signals, while also reducing the high path loss associated with higher frequencies. Due to their versatile nature, antenna arrays produce various beam patterns, which allows for freedom in adjusting the transmission power and direction [4]. The degrees of freedom that benefit antenna arrays are due to weighting the phase and amplitude of different channels across the antenna array. This freedom ensures a radiation pattern with sidelobes adjusted to form nulls in the direction of interferers, while the mainlobe remains unchanged.

1.1 Problem Description

The emergence of new technology has much potential use in new applications but, such potential can not be fulfilled without the reemergence of old existing problems; one such problem is the near-far problem [5]. The near-far problem is as old as communication itself. It entails that the receiver is rather limited in detecting a weak signal when a strong signal is simultaneously received. The strong signal blocks the weak signal, causing unacceptable interference at the receiver end.
In an IAB node, access and backhaul share the same spectrum. This leads to the possibility of interference from undesired signals, also known as jammers. Thus, to suppress jamming signals, interference rejection methods must be deployed. This would include adjusting the antenna radiation pattern so that nulls manifest in the direction where the jammers are found.
Nulling in a certain direction prevents interference only if the jamming signals re-

main in that direction. However, in a time-varying environment, jammers can come from any direction at any time. This could be due to a sudden change in the utilized spectrum or an intentional jammer. Thus, an antenna array will need to continuously adapt its weights to be able to cancel the jammer. This adaptive property is not without its challenges especially if the signal processing capability is limited as is the case in analog arrays [7]. Figure 1.1 shows a beam pattern with a mainlobe

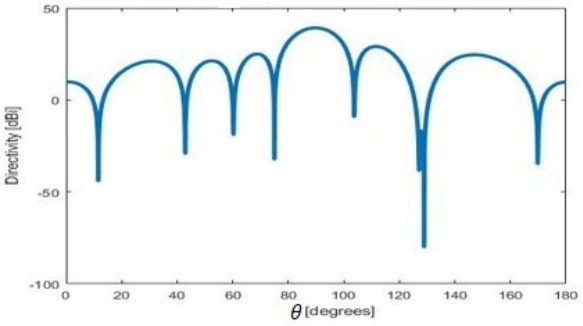

(a) Radiation Beam pattern

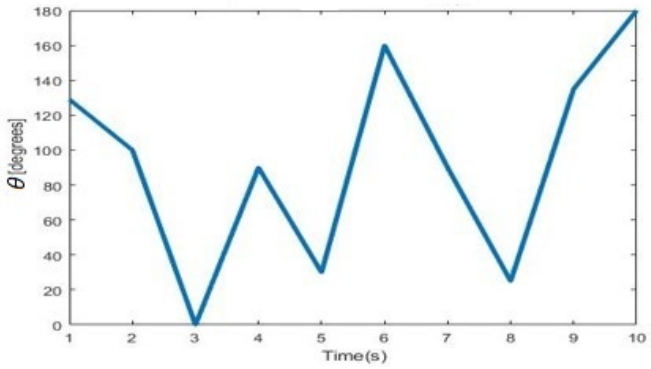

(b) Jammers Angle of Arrival

set at 90 degrees. The pattern consists of 7 nulls scattered from 0 to 180 degrees. However, the null found at 129 degrees has been produced to minimize the effect of any jamming signal arriving at 129 degrees. Figure 1.1(b) represents the different jammers and the corresponding angles of arrival that can be expected from a time-varying environment. Thus, the antenna array will need to adjust its beam pattern accordingly to accommodate for jammers having different angles of arrival. While adjusting, the antenna array needs to maintain the beam pattern such that the mainlobe is unchanged in shape and direction.
Precoding in digital massive MIMO encodes antenna signals to form complex radiation patterns both spatially and in the time domain [8]. These radiation beam patterns however are not clearly defined, and consequently, the adaptive property described can not be applied in the same way.

1.2 Related Works

Adaptive arrays are used extensively in both radar and communication applications, whether it is to null interfering sources or reduce radar clutter [6, 7]. The factors that govern the effectiveness of an adaptive array include the number of array elements, the antenna aperture diameter, the location of the interfering sources and finally the algorithm or precoding algorithm utilized in the adaptive array. The Applebaum algorithm is one of the oldest of such algorithms. As such, its center principle from which adaptation is achieved has often been used as a reference point to similar algorithms that came later on. The algorithms do however vary in effectiveness depending on the scenario, application, and type of array used [7].
Adaptive antenna arrays vary in architecture. They usually include low noise amplifiers, analog filters, a radio frequency stage, an intermediate frequency stage, down-converters and finally an analog to digital converter and a digital signal processor. Based on the particular architecture, antenna arrays can be classified as either analog or digital arrays [7]. Precoders like zero forcing or minimum mean squared error are of efficient use in digital arrays, but due to inexpensive phase shifters, it is often preferable to use analog or hybrid beamforming when possible, to which old radar algorithms like the Applebaum algorithm or the Sample Matrix Inversion (SMI) algorithm seem to yield efficient results [8].

1.3 Scope of Thesis

The purpose of this thesis is to use the current simulation platform provided by Huawei research center to implement the Applebaum algorithm. By going through Applebaum's paper [9] in a step by step manner, this thesis aims to grasp and covey an adequate understanding regarding the functionality of the algorithm. The covariance matrix is an important mathematical tool that can be used in antenna arrays to capture the nature of the noise environment produced by different jammers. The Applebaum algorithm uses the covariance matrix to derive a control law for adaptation to jammers. How well this control law works is judged by system performance metrics like the Signal to Noise Ratio (SNR), Signal to Interference and Noise Ratio (SINR) and the SINR improvement. Simulations for different jamming signal strengths, Angle of Arrival (AoA) and radiation patterns are run to properly conclude the effectiveness and the limitations of the algorithm.

2
Theory

2.1 5G: New Radio

In today's world, cellular access can be granted to almost anyone at any time. A networked society driven by 5G new radio (NR) aims to also extend this possibility to things [17]. This would then cause huge growth in the number of connected devices and the corresponding traffic would be of overwhelmingly high proportion. To address these circumstances, 5G enables new functionality and provides more spectrum [16]. This involves using mm-wave frequency bands, that are currently unemployed. 5G: NR aims to cover frequencies from 1 GHz to 100 GHz; as a consequence, the architecture for antenna arrays will differ in order to properly accommodate this frequency range [16]. The technical specifications required to enable 5G NR are solely in the hands of the 3rd Generation Partnership Project (3GPP), a project which started in 1998 and is now responsible for collaborations between various regional and national standard development organizations [16]. 3GPP specifications consist of different releases, where each release includes a complete set of specifications. Furthermore, 3GPP aims to initiate global standards for 5G by finalizing the specifications needed for new spectrum between 6-100 GHz (5G: NR), while also including current existing spectrum from 1 to 6 GHz (LTE evolution) [16]. The International Telecommunications Union- Radio (ITU-R) are then responsible to turn the specification provided by 3GPP into global standards, while also providing feedback and recommendations regarding the specifications and the potential technologies associated [16].

2.1.1 Integrated Access and Backhaul

An access link enables Base Stations (BS) to provide mobile users with their required data, while a backhaul link enables base stations to send communication data, through nodes, to the central network. In current generation wireless networks, backhaul is often found to be fiber-based and also fixed in its spectrum allocation; however, since 5G consists of many Self Backhaul Small Cells (SBSc), deploying fiber to each cell would be costly, time-consuming and inefficient [2, 18]. Because 5G utilizes higher frequencies, it benefits from more spectrum and directive beamforming. These properties found in 5G allow for the possibility of using fixed wireless backhaul links for SBSc instead of fiber-based backhaul links [18]. Fixed wireless backhaul is however insufficient, in so far that traffic demands can not be met. For instance, if traffic demand increases in one part of an SBSc cell, the fixed bandwidth in access and backhaul can not be used to compensate for this increase in

demand. Furthermore, an integrated access and backhaul approach (i.e sharing the same spectrum), becomes very beneficial, as it not only enables flexible and dense deployment of SBSc stations but also does so without densifying the transport network proportionally [2, 3]. Figure 2.1 shows the links for an IAB node. From Figure 2.1, the parent node (P), child node (C), and the mobile user have a total of 6 links to the IAB node (A). IAB supports Time-Division-Multiplexing (TDM) as well as Frequency-Division-Multiplexing (FDM). When TDM is used a total of 16 cases is supported [3].

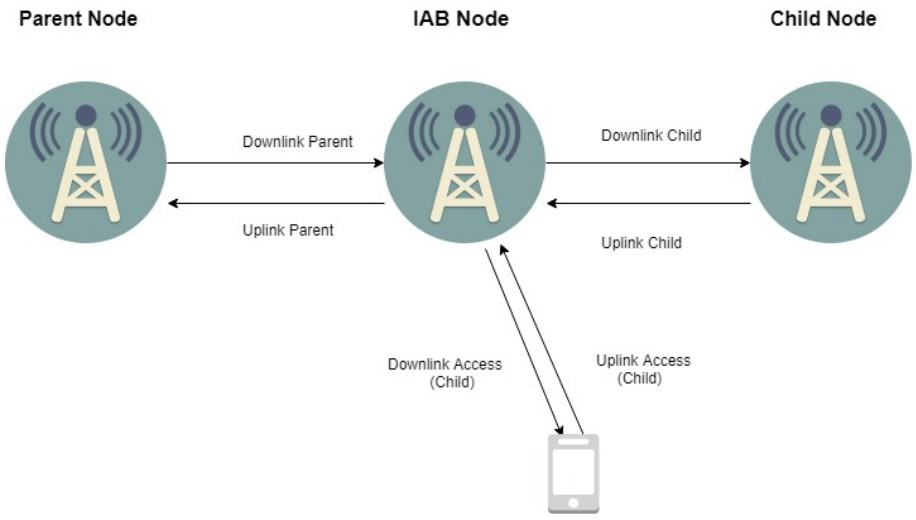

Figure 2.1: Links in IAB [3]

TDM Between:		
Case	Link 1	Link 2
1	LP,DL	LC,DL
2	LP,UL	LC,UL
3	LP,DL	LC,UL
4	LP,UL	LC,DL
5	LP,DL	LA,DL
6	LP,UL	LA,UL
7	LP,DL	LA,UL
8	LP,UL	LA,DL
9	LP,DL	LA,DL and LC,DL
10	LP,UL	LA,UL and LC,UL
11	LP,DL	LA,UL and LC,UL
12	LP,UL	LA,DL and LA,DL
13	LC,DL	LA,DL
14	LC,UL	LA,UL
15	LC,DL	LA,UL
16	LC,UL	LA,DL

Table 2.1: TDM links in IAB

One drawback of IAB is that since access and backhaul share the same spectrum, there is a likelihood of interference between the child, parent and access links. Thus, IAB requires sufficient interference rejection methods to suppress interference.

2.2 Multiantenna Techniques

Multiantenna techniques have been used in both current and previous generations of wireless systems, but in 5G, their role is more fundamental to the system design [16]. A wireless channel causes a variety of detrimental effects to a transmitting signal, these include path loss, long-term fading, short term fading, co-channel interference, adjacent channel interference, intersymbol interference, and increase in receiver noise [19]. Multiantenna techniques are used to minimize these effects. These multiantenna techniques include beamforming, precoding, and interference suppression that coherently combine multiple antenna elements in either the transmitter, receiver or in some cases both to achieve different gains [16].
The most simple multiantenna technique is beamforming. By using an array of elements, beamforming focuses radio energy in a particular direction. By applying time delays to the antenna elements, the signals of different antenna elements add constructively in a certain direction, increasing the overall gain, known as the array gain [16]. This technique is indeed useful when it comes to a Line of Sight (LoS) channel, but when signal reflections cause a multipath propagation channel then the rays have different angles of arrival as well as various phases and amplitudes and so forming a single beam is no longer ideal [16]. For such cases, the optimal becomes to combine the antenna elements in such a way that the desired signals can be aligned and constructively added at the receiver side [16]. This technique is known as precoding and requires a DSP for each antenna element (digital array). Unlike beamforming, precoding can also include a diversity gain by reducing the effect of fading through the combination of different antenna elements that experience different fading [16]. The techniques used to mitigate interferers while transmitting to a user differ depending on the kind of channel. Generally, non-LoS channels use the channel transfer function to produce nulls in the direction of interferers, while LoS scenarios that perform nulling in the analog domain use the covariance matrix or gradient-based methods to null jammers [25].
Because 5G deals with low and high frequency, the multiantenna techniques employed vary from previous technologies. New techniques have been introduced for frequencies above 24 GHz, named as FR2 [20]. At higher frequencies more antenna elements can be fit into a smaller surface area, so the beamforming becomes more directive. Unlike previous generations, beamforming at higher frequencies is possible for control and broadcast signals as well as data transmission [16]. To properly reap the benefits of multiantenna techniques, the antenna system designer needs to take into account the hardware implementation required to successfully combine multiple antennas. This includes the architecture of the antenna array.

2.2.1 Precoding with Digital Arrays

Digital arrays include RF chains, with data converters for each antenna element as Figure 2.2 shows. This allows for a lot of flexibility when combining antenna elements and thus, more degrees of freedom in signal processing [16]. Multiantenna techniques are then more easily implemented and even reach their full potential. Thus, through having sophisticated receivers and precoders, the required signal processing for interference suppression is easily managed [16].

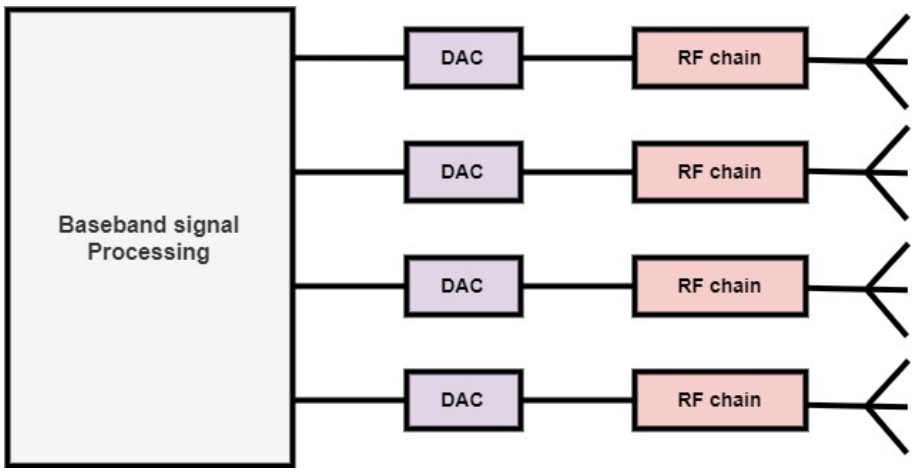

Figure 2.2: Digital Array Architecture [16]

Although nonlinear processing techniques like dirty paper coding can be optimal, they often entail more complexity in the transmitter and receivers end [21, 22]. Hench, the receivers and precoders more widely in use prefer linear processing techniques to reduce complexity in detection and precoding [21]. These techniques include Zero-Forcing (ZF), Minimum Mean Squared Error (MMSE) and Maximum Ratio Combing (MRC) for downlink or Maximum Ratio Transmission (MRT) for uplink. These techniques use the channel transfer function ($\boldsymbol{H}$) between users and a BS antenna array with K number of antennas. The channels are generally modeled by large scale fading and small scale fading [21].
According to [21, 23, 24], a typical multi-user MIMO system with K antennas at the BS has an uplink transmission, which entails transmission from the user to the BS, as follows:

$$\begin{aligned} \boldsymbol{y}^{\mathrm{ul}} &= \sqrt{p_{\mathrm{u}}} \sum_{n=1}^{N} \boldsymbol{h}_n s_n + \boldsymbol{n} \\ &= \sqrt{p_{\mathrm{u}}} \boldsymbol{H} \boldsymbol{s} + \boldsymbol{n}, \end{aligned} \tag{2.1}$$

where $\boldsymbol{s} = [s_1, s_2..., s_n]^T$and $\boldsymbol{n} \in \mathbb{C}^{K \times 1}$ where, $\boldsymbol{n} \sim CN(\boldsymbol{0}_K, \boldsymbol{I}_K)$.

Furthermore, N in (2.1) is the number of users, p_u denotes the average SNR, s_n refers to the signal transmitted from the nth user, while $\boldsymbol{h}_n$ is the channel response for the nth user. The additive noise vector is represented as $\boldsymbol{n}$, with the assumption of zero mean and unit variance. The bold upper case letters of (2.1) represents a matrix, while the lower bold case letters represent vectors; non bold lower case letters denote scalars. The received signal $\boldsymbol{y}^{\mathrm{ul}}$ tends to $\tilde{\boldsymbol{y}}^{\mathrm{ul}}$,

$$\tilde{\boldsymbol{y}}^{\mathrm{ul}} = \boldsymbol{A}^H \boldsymbol{y}^{\mathrm{ul}} = \sqrt{p_{\mathrm{u}}} \boldsymbol{A}^H \boldsymbol{H} \boldsymbol{s} + \boldsymbol{A}^H \boldsymbol{n}, \tag{2.2}$$

as it enters through K antennas; thus, $\boldsymbol{y}^{\mathrm{ul}}$ has K dimensions. As shown in (2.2), $\boldsymbol{y}^{\mathrm{ul}}$ is then multiplied by a linear detection matrix $\boldsymbol{A} \in \mathbb{C}^{K \times N}$ and thus separated into N streams for N users, where each stream is decoded separately. The received signal after combining for the nth user $\tilde{y}_n^{\mathrm{ul}}$ can be written as:

$$\tilde{y}_n^{\mathrm{ul}} = \underbrace{\sqrt{p_{\mathrm{u}}} \boldsymbol{a}_n^H \boldsymbol{h}_n s_n}_{\text{desired signal}} + \underbrace{\sqrt{p_{\mathrm{u}}} \sum_{n' \neq n}^{N} \boldsymbol{a}_n^H \boldsymbol{h}_{n'} s_{n'}}_{\text{interuser interference}} + \underbrace{\boldsymbol{a}_n^H \boldsymbol{n}}_{\text{noise}}. \tag{2.3}$$

It is easy to see from (2.3), that the SINR for the nth user is given as:

$$\mathrm{SINR}_n = \frac{p_{\mathrm{u}} \left| \boldsymbol{a}^H \boldsymbol{h}_n \right|^2}{p_{\mathrm{u}} \sum_{n' \neq n}^{N} \left| \boldsymbol{a}_n^H \boldsymbol{h}_{n'} \right|^2 + \left\| \boldsymbol{a}_n \right\|^2}. \tag{2.4}$$

The different linear processing techniques tweak different parameters of (2.4) in order to maximize the SINR. The MRC receiver for instance aims to maximize the desired signal with respect to the noise (SNR).

$$\begin{aligned} \boldsymbol{a}_n^{\mathrm{mrc}} &= \underset{\boldsymbol{a}_n \in \mathbb{C}^{K \times 1}}{\operatorname{argmax}} \frac{\text{power (desired signal)}}{\text{power (noise)}} \\ &= \underset{\boldsymbol{a}_n \in \mathbb{C}^{K \times 1}}{\operatorname{argmax}} \frac{p_{\mathrm{u}} \left| \boldsymbol{a}_n^H \boldsymbol{h}_n \right|^2}{\left\| \boldsymbol{a}_n \right\|^2}, \end{aligned} \tag{2.5}$$

using the Cauchy-Schwartz inequality,

$$\frac{p_{\mathrm{u}} \left| \boldsymbol{a}_n^H \boldsymbol{h}_n \right|^2}{\left\| \boldsymbol{a}_n \right\|^2} \leq \frac{p_{\mathrm{u}} \left\| \boldsymbol{a}_n \right\|^2 \left\| \boldsymbol{h}_n \right\|^2}{\left\| \boldsymbol{a}_n \right\|^2} = p_{\mathrm{u}} \left\| \boldsymbol{h}_n \right\|^2. \tag{2.6}$$

This equality holds when $\boldsymbol{a}_n = \text{const} \times \boldsymbol{h}_n$. Thus, substituting $\boldsymbol{a}_n = \text{const} \times \boldsymbol{h}_n$, the SINR, with increasing SNR tends to:

$$\begin{aligned} \mathrm{SINR}_n^{\mathrm{mrc}} &= \frac{p_{\mathrm{u}} \left\| \boldsymbol{h}_n \right\|^4}{p_{\mathrm{u}} \sum_{n' \neq n}^{N} \left| \boldsymbol{h}_n^H \boldsymbol{h}_{n'} \right|^2 + \left\| \boldsymbol{h}_n \right\|^2} \\ &\to \frac{\left\| \boldsymbol{h}_n \right\|^4}{\sum_{k' \neq n}^{N} \left| \boldsymbol{h}_n^H \boldsymbol{h}_{n'} \right|^2}, \text{ as } p_{\mathrm{u}} \to \infty. \end{aligned} \tag{2.7}$$

Instead of maximizing the SNR, the ZF technique aims to eliminate the interuser interference. This is achieved by having a ZF receiver matrix which satisfies:

$$\begin{cases} \boldsymbol{a}_{\mathrm{zf},n}^H \boldsymbol{h}_n \neq 0 \\ \boldsymbol{a}_{\mathrm{zf},n}^H \boldsymbol{h}_{n'} = 0, \quad \forall n' \neq n. \end{cases} \tag{2.8}$$

The ZF forcing matrix ($\boldsymbol{a}_{\mathrm{zf},n}^H$) capable of satisfying (2.8), is the psudo-inverse of the channel matrix given as: $(\boldsymbol{H}^H \boldsymbol{H})^{-1} \boldsymbol{H}^H$ [21]. Thus, the received signal becomes:

$$\tilde{\boldsymbol{y}}^{\mathrm{ul}} = \left(\boldsymbol{H}^H \boldsymbol{H} \right)^{-1} \boldsymbol{H}^H \boldsymbol{y}^{\mathrm{ul}} = \sqrt{p_{\mathrm{u}}} \boldsymbol{s} + \left(\boldsymbol{H}^H \boldsymbol{H} \right)^{-1} \boldsymbol{H}^H \boldsymbol{n}, \tag{2.9}$$

and the SINR for the nth user becomes:

$$\mathrm{SINR}_{\mathrm{zf},n} = \frac{p_{\mathrm{u}}}{\left[\left(\boldsymbol{H}^H\boldsymbol{H}\right)^{-1}\right]_{nn}}. \tag{2.10}$$

The MMSE minimizes the estimated signal error with respect to the transmitted signal as follows:

$$\boldsymbol{A}^{\mathrm{mmse}} = \underset{\boldsymbol{A}\in\mathbb{C}^{K\times N}}{\operatorname{argmin}}\, \mathbb{E}\left\{\left\|\boldsymbol{A}^H\boldsymbol{y}^{\mathrm{ul}} - \boldsymbol{s}\right\|^2\right\} = \underset{\boldsymbol{A}\in\mathbb{C}^{K\times N}}{\arg\min} \sum_{n=1}^{N} \mathbb{E}\left\{\left|\boldsymbol{a}_n^H\boldsymbol{y}^{\mathrm{ul}} - s_n\right|^2\right\}. \tag{2.11}$$

Thus, the MMSE technique finds the $\boldsymbol{a}_n$ that minimizes (2.11), where $\boldsymbol{a}_n$ is the nth column of $\boldsymbol{A}$. By noting that the covariance $\mathrm{cov}\left(\boldsymbol{v}_1, \boldsymbol{v}_2\right) \triangleq \mathbb{E}\left\{\boldsymbol{v}_1\boldsymbol{v}_2^H\right\}$, the n:th column of the MMSE reciever matrix ($\boldsymbol{a_n}^{\mathrm{mmse}}$) is:

$$\begin{aligned}
\boldsymbol{a}_n^{\mathrm{mmse}} &= \underset{\boldsymbol{a}_n\in\mathbb{C}^{K\times 1}}{\arg\min}\, \mathbb{E}\left\{\left|\boldsymbol{a}_n^H\boldsymbol{y}^{\mathrm{ul}} - s_n\right|^2\right\} \\
&= \mathrm{cov}\left(\boldsymbol{y}^{\mathrm{ul}}, \boldsymbol{y}^{\mathrm{ul}}\right)^{-1} \mathrm{cov}\left(s_n, \boldsymbol{y}^{\mathrm{ul}}\right) \\
&= \sqrt{p_{\mathrm{u}}}\left(p_{\mathrm{u}}\boldsymbol{H}\boldsymbol{H}^H + \boldsymbol{I}_K\right)^{-1}\boldsymbol{h}_n.
\end{aligned} \tag{2.12}$$

Thus, the resulting SINR for MMSE becomes:

$$\mathrm{SINR}_n^{\mathrm{mmse}} = p_{\mathrm{u}}\boldsymbol{h}_n^H\left(p_{\mathrm{u}}\sum_{i\neq n}^{N}\boldsymbol{h}_i\boldsymbol{h}_i^H + \boldsymbol{I}_K\right)^{-1}\boldsymbol{h}_n. \tag{2.13}$$

When the BS antenna array is transmitting and the users are receiving, the communication is denoted as downlink. As a result, the SINR equation shall differ from (2.1). However, the techniques covered for the antenna array receiver (uplink) are also similar to the precoders (downlink) for the antenna array transmitter. The formulas attaining to these precoders are shown below by a precoding matrix denoted as $\boldsymbol{P}$,

$$\boldsymbol{P} = \begin{cases} \boldsymbol{H}^*, & \text{for MRT} \\ \boldsymbol{H}^*\left(\boldsymbol{H}^T\boldsymbol{H}^*\right)^{-1}, & \text{for ZF} \\ \boldsymbol{H}^*\left(\boldsymbol{H}^T\boldsymbol{H}^* + \frac{N}{p_{\mathrm{d}}}\boldsymbol{I}_N\right)^{-1}, & \text{for MMSE}, \end{cases} \tag{2.14}$$

where p_{d} denotes the average SNR for downlink. The different linear processing techniques all have certain advantages and disadvantages, Table 2.2 below summarises them:

Table 2.2: Properties of different digital precoders

Scheme	MRT/MRC	ZF	MMSE
Advantages	Achieves high array gain even at low SNR.	Can easily tweak the SINR, works well in interference scenerios.	Trades interference suppression against signal power efficiency, outperfoms ZF and MRT
Disadvantages	Ignores interuser interference term which limits performance in scenerios with high interference.	Noise in reciever is drastically higher due to the psudo-inverse matrix.	Higher complexity, lower performance capability when SNR is low.

The techniques explored so far were derived under the assumption of perfect Channel State Information (CSI). CSI describes the channel state. In general, CSI can be more or less known by the transmitter or the receiver. The acronym CSIT denotes the CSI at the transmitter while CSIR represents CSI at the receiver. Thus, perfect CSIR or CSIT entails that the receiver or transmitter has complete knowledge of the channels state. However, in practical systems, the CSIR or CSIT is not perfect [21]. There are a number of different algorithms used to estimate the CSI using pilot signals. In the case of precoding, CSIT is required. Furthermore, depending on the CSIT available, the utility of using one precoder over the other may vary [23, 24].

2.2.2 Precoding with Analog Arrays

Analog arrays differ from digital arrays in architecture. While digital arrays include an RF chain and data converters for each antenna element, analog arrays have a common RF chain and a converter. In addition, analog arrays use phase shifters and gain control for beamforming and amplitude tapering [16].

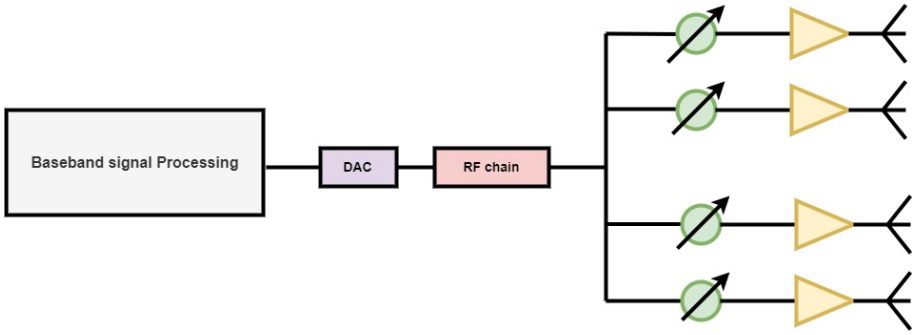

Figure 2.3: Analog array architecture [16]

Figure 2.3 shows the architecture at the transmitter side for an analog array [16]. Analog arrays lack the signal processing capabilities of a digital array, and as a consequence, they are usually limited to analog beamforming. Furthermore, because

analog arrays are unable to adapt to the frequency selectivity of the channel, they are better suited for environments with less scattering and a higher likelihood for LOS. Fortunately, the probability for LOS is high for mm-wave small base stations (SBSC) deployed in 5G [16]. Due to its directional nature, analog beamforming is very susceptible to interfering signals. Analog arrays overcome this constraint by beamforming in an adaptive manner. Adaptive beamforming or adaptive arrays have been around and studied since the 1950s and have been used in many applications, especially radar [7, 25]. Adaptive beamforming comprises different algorithms capable of tweaking the amplitude and phase of each antenna element. The tweaks then adjust the antenna radiation pattern to have nulls in the direction of interfering signals; thus, maintaining the gains in the direction of the desired signal while simultaneously maximizing attenuation in the direction of the interfering signal [7, 25]. In an adaptive analog array with K elements, the weighted signals at each element are summed. The element weights are complex numbers, which are then tweaked to achieve a desired radiation pattern accordingly. Thus an array with K elements have K degrees of freedom, wherein K-1 degrees of freedom can be used for creating nulls. In [7] it is shown that the signal output y of an adaptive array can be written as:

$$y = \boldsymbol{w}^T \boldsymbol{s} = \boldsymbol{s}^T \boldsymbol{w}, \tag{2.15}$$

where $\boldsymbol{w}$ represents a weighting vector while $\boldsymbol{s}$ denotes a complex signal input vector and T refers to transpose. By taking the expected value, the output power tends to

$$\mathbb{E}\{|y|^2\} = \mathbb{E}\{\boldsymbol{w}^T \boldsymbol{s}^* \; \boldsymbol{s}^T \boldsymbol{w}\Big\} = \boldsymbol{w}^T \mathbb{E}\left\{\boldsymbol{s}^* \boldsymbol{s}^T\right\} \boldsymbol{w} = \boldsymbol{w}^T \mathbb{E}\left\{\boldsymbol{s}\boldsymbol{s}^H\right\} \boldsymbol{w} = \boldsymbol{w}^T \boldsymbol{R} \boldsymbol{w}. \tag{2.16}$$

Here, $\boldsymbol{R}$ represents the covariance matrix of the input signal. The covariance matix is a very important matrix in some adaptive arrays. The covariance matrix contains important contributions of the user signal, jamming signal and receiver noise, all from which an algorithm can be produced [7]. However, not all the algorithms use the covariance matrix to suppress interfering signals. The algorithms employed in adaptive beamforming usually belong to one of three classes of algorithms. The first class uses a method of steepest descent and belongs to the Least Mean Squared (LMS) family. This family of algorithms is regarded as gradient-based algorithms, as they employ a noisy estimate of the required gradient vector [25]. The second class is hinted above and comprises a family of matrix inversion algorithms that manipulate the covariance matrix or correlation matrix of a desired input signal, jamming input signal or the noise component of the antenna elements at the antenna array [25]. Finally, the third class of algorithm consists of algorithms that use the stochastic approximation of the Guass-Newton method and is known as the Recursive Least Squares (RLS) family [25]. Table 2.3 below summarizes some of the popular algorithms used for adaptive beamforming. These algorithms have the following properties [25].

Algorithm	LMS	SMI	Applebaum
Working Principle	Minimizes the mean square error with the use of reference signal	Estimates array vector weights using a correlation matrix	Estimates array vector weights using a covarience matrix
Advantages	Low complexity, better stability	Fast covergence rate	Easy to implement
Disadvantages	Slow convergence, require reference signal.	A priori knowledge of the arrival angle, higher complexity	A priori knowledge of the arrival angle, more succesptible to errors.

Table 2.3: Properties of different adaptive array algorithms

2.3 Antenna arrays

Unlike an ordinary antenna, antenna arrays are able to shape and steer their beam patterns in various directions by tweaking the phase excitation of the array elements [11]. This property of arrays makes them very useful for various applications, whether for commercial, personal or military use [12].
The Yagi-Uda array was one of the very first antenna arrays used in 1926 [11]. It was configured to have only one driver element connected to a transmitter or receiver, while the other elements were parasitic and contributed to the overall radiation pattern by the incident radiation pattern emerging from the driver element [11]. More such antennas emerged during world war 2, but it was not until the 1950s, with the invention of the ferrite phase shifter that electronic scanning became possible and thus, the arrival of phased antenna arrays [11].
In antenna arrays, the total radiated field pattern depends not only on the individual element field patterns but also on the displacement between these elements, the relative phase and amplitude of each element, and the geometrical configuration of the overall array [12]. Thus, antenna arrays have many degrees of freedom and can often be steered and shaped in accordance to a desired field pattern.

2.3.1 Antenna Radiation patterns

Figure 2.4 below shows the geometry for a 2 element array. The first antenna element is located to the left of the origin, whilst the second antenna element is to the right of the origin. The two elements are separated at a distance d. The angle ϕ , is the angle of arrival for rays emerging from the far field and the distance X, is the extra distance a ray travels to reach element 1 relative to element 2. Through basic trigonometry $X = d\cos\phi$.

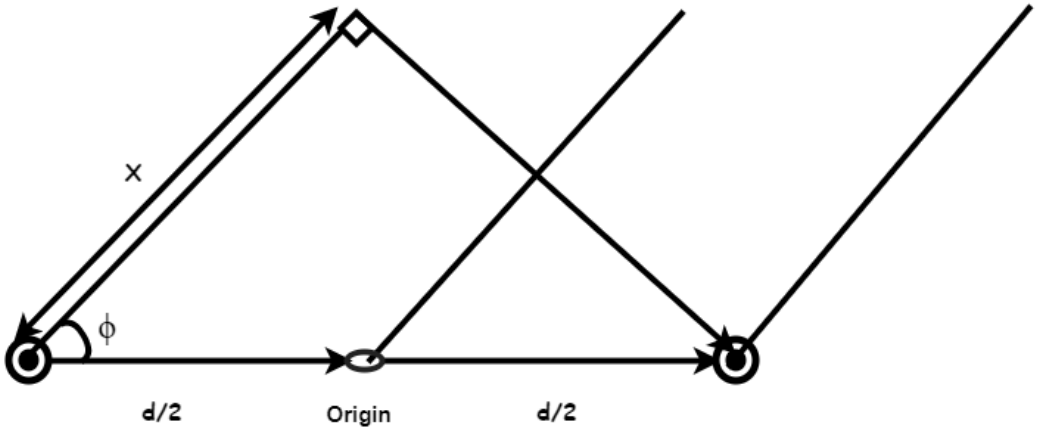

Figure 2.4: Geometry for Two Element Array [12]

This translates to a phase difference of

$$d_{Phase} = (\frac{2\pi}{\lambda})(d\cos\phi), \tag{2.17}$$

where λ is the wavelength of the emerging ray. Accounting for an initial phase α, (2.17) tends to $(2\pi/\lambda)\, d\cos\phi + \alpha$. By using identical isotropic elements, the electric field of element 1 and element 2 can be set to E_0. From Figure 2.4 it is easy to observe that element 1 and 2 lag or lead by $\frac{\Phi}{2}$ with respect to the origin, where Φ denotes the phase difference $(2\pi/\lambda)\, d\cos\phi + \alpha$. Thus, the total electric field can be derived as follows:

$$E_{total} = E_0 e^{j\frac{\Phi}{2}} + E_0 e^{-j\frac{\Phi}{2}} = 2E_0 \frac{(e^{j\frac{\Phi}{2}} + e^{-j\frac{\Phi}{2}})}{2} = 2E_0 \cos(\frac{\Phi}{2}). \tag{2.18}$$

Thus, (2.18) shows that the electric field E_0 is multiplied by a factor $2\cos\frac{\Phi}{2}$. This factor is known as the Array Factor (AF).
In general, if the elements in the array are identical, the electric field pattern of any antenna array can be found by (2.19) [12].

$$E_t = E_0 \times AF, \tag{2.19}$$

where E_t and E_0 stand for the total electric field and the electric field from a single identical element. The AF expresses the nature of the antenna array. For antenna arrays, the AF is unique and represents the properties of an array, such as the arrays geometry, relative spacing and relative phase of the elements [12].
For instance, when the elements of an array are identical isotropic point sources with relative power of 1 dB, different AF will influence the resultant radiation pattern. By changing the relative phase and spacing of the elements, the AF of the array changes and as a result, different radiation patterns emerge. Figure 2.5 shows these phenomena; thus, the resultant radiation pattern of the array varies when the phase α remains the same but the spacing between the elements are changed. Consequently, Figure 2.5(a) has its mainlobe at 90 and 270 degrees and form nulls

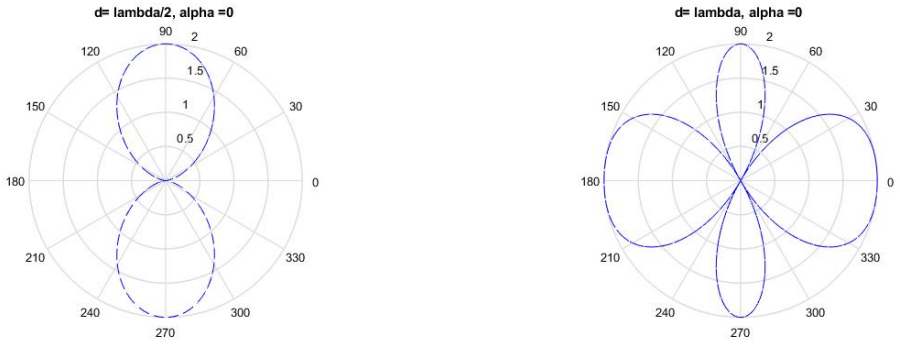

(a) (b)

Figure 2.5: Radiation pattern for two element array

at 0 and 180 degrees, while Figure 2.5(b) form nulls 60, 120, 240, 300 and has its mainlobe at 0 and 180 degrees. On the other hand, Figure 2.6 shows what happens when the spacing is kept constant and the phase α varies. It can be observed that the resulting radiation patterns of Figure 2.6(a) and 2.6(b) are opposite.

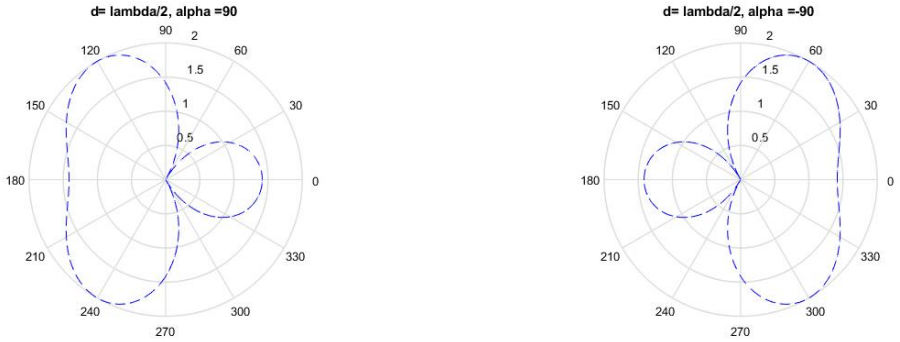

(a) (b)

Figure 2.6: Radiation pattern for two element array

2.3.2 Uniform Linear array

The geometry of linear arrays consists of K antenna elements, each with different phase shifts, placed along a line [12]. When those phase leads are progressive, the array is known as a uniform linear array [12]. In such arrays the array factor AF is given by:

$$AF = \sum_{k=1}^{K} e^{j(k-1)((2\pi d/\lambda)\cos(\phi)+\alpha)} = \sum_{k=1}^{K} e^{j(k-1)(\Phi)}. \tag{2.20}$$

By further mathematical manipulation and expansion, (2.20) can be normalized and

written as:

$$(AF)_n = \frac{\sin\frac{K\Phi}{2}}{\frac{K\Phi}{2}}, \tag{2.21}$$

where the subscript n denotes normalization. Setting (2.21) to zero, the nulls of the antenna can be found and furthermore, the resulting radiation pattern. It then becomes possible to direct the beam pattern for any uniform linear array by tweaking parameters inherent in Φ. In some applications there is a need to focus the radiated energy in a certain direction. This can be achieved by choosing a single element that has a maxima in a certain direction and setting the array factor such that the same maxima is obtained in the same direction as the radiating element [12].

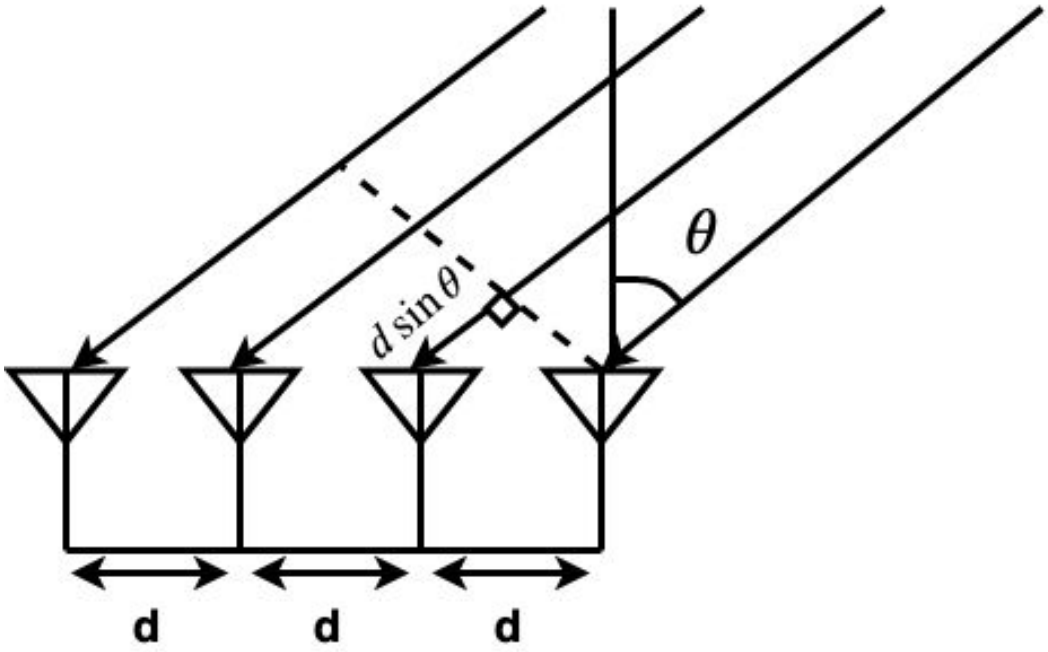

Figure 2.7: Geometry for a uniform linear array [13]

Figure 2.7 shows a far field incident array arriving at an angle θ to the normal of a uniform linear array. Here a vector $\boldsymbol{b}$ is used to compensate for the lag of $d\sin\theta$, such that the received signal can be combined coherently:

$$\boldsymbol{b} = \begin{pmatrix} 1 \\ e^{-i\beta} \\ e^{-i2\beta} \\ . \\ . \\ . \\ e^{-i(K-1)\beta} \end{pmatrix}, \tag{2.22}$$

where $K-1$ are the number of phase shifts which are multiples of $\beta = (2\pi d/\lambda)(\sin\theta)$ that are applied progressively to each element in the array.

2.3.2.1 Uniform Linear arrray: Wideband

When the $\boldsymbol{b}$ vector is applied to a wideband signal, a beam squint occurs. A beam squint causes a change in the beam direction as a function of frequency and because a wideband signal consists of a range of frequencies, the $\boldsymbol{b}$ vector will cause a phase error to occur when applied to wideband signals [14, 15]. This phase error, denoted as e_{ph}, is calculated in (2.23), by subtracting the phase shift applied to the center frequency (f_0), from the phase shift applied at the band edge frequency (f) for a particular element k, where θ_0, θ correspond to angles for f_0, f respectively.

$$e_{ph} = \frac{2\pi f}{c} dk \sin(\theta) - \frac{2\pi f_0}{c} dk \sin(\theta_0) = (\frac{2\pi f}{c} dk)(\sin(\theta) - \frac{f_0}{f} \sin(\theta_0)). \tag{2.23}$$

Thus, e_{ph} in (2.23) becomes 0 when $\sin(\theta) = \frac{f_0}{f} \sin(\theta_0)$. Thus wideband signals introduces an offset distance of: $\Delta d \sin(\theta_{offset}) = \sin(\theta_0) - \frac{f_0}{f} \sin(\theta_0) = \sin(\theta_0)(1 - \frac{f_0}{f})$.

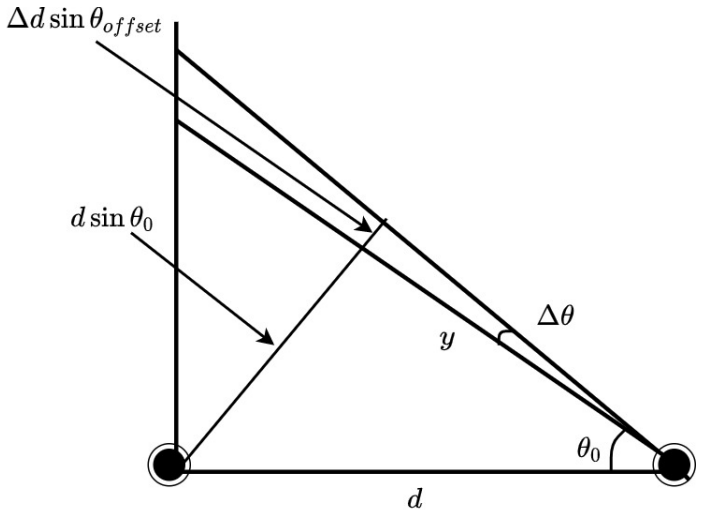

Figure 2.8: Pointing offsett for a wideband signal

Figure 2.8 shows that the offset distance $\Delta d \sin(\theta_{offset})$ consists of a pointing error $\Delta\theta$ which through basic trigonometry can be found as:

$$\begin{aligned} \frac{\Delta d \sin(\theta_{offset})}{y} &= \tan(\Delta\theta) \\ \text{where, } \tan(\Delta\theta) &= \Delta\theta \\ \cos(\theta_0) &= \frac{y}{d}, \\ \text{thus, } \Delta\theta &= \frac{\Delta d \sin(\theta_{offset})}{\cos(\theta_0)}. \end{aligned} \tag{2.24}$$

2.4 The Applebaum Algorithm

The Applebaum algorithm is often regarded as a Parent algorithm for interference suppression. Applebuam introduced his algorithm in 1976 and since then it has been reprinted and studied due to the reoccurring interest in the field of interference suppression [9]. The Applebaum algorithm was produced for uniform linear arrays and achieves interference suppression in the analog domain by maximizing the SNR of an antenna array [25, 9]. In [9] Applebaum expounds on how this criteria (SNR) can be used to derive a control law $\boldsymbol{Mw} = \mu \boldsymbol{s}^*$, where $\boldsymbol{M}$ is the covariance matrix of the noise components at the antenna elements and $\boldsymbol{w}$ is the weight vector for the current noise environment. μ is an arbitrary constant and $\boldsymbol{s}^*$ is the desired signal assumed to be present in K channels in proportion to known complex numbers. This control law adapts new weights for new noise environments. The derivation for the control law can be understood by analyzing the same antenna array from two different perspectives, with and without a transformation matrix $\boldsymbol{A}$.

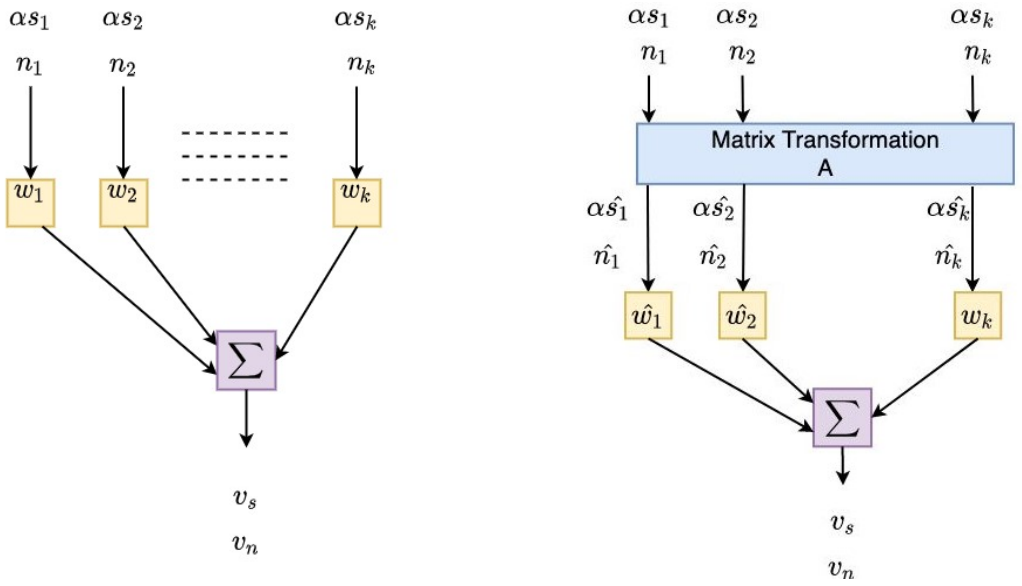

(a) Array without transformation

(b) Array with transformation

Figure 2.9: Block diagram for the Applebaum Algorithm [9]

Figure 2.9 represents a linear uniform antenna array with K elements depicted through two equivalent block diagrams. Here αs_k represents the desired signal entering the kth element of the array, where α is the time and amplitute variation of the signal. n_k represents the receivers background thermal noise and the spatial distribution of all noise sources (jammers) seen by the kth antenna element. Figure 2.9 (b) includes a transformation matrix $\boldsymbol{A}$ which will later be shown to maximize the SNR ($|v_s|^2/\mathbb{E}\{|v_n|^2\}$) by deccorelating the antenna elements noise powers at the array output. The noise power at the output of the kth antenna element is denoted as ν_{kk}, while ν_{kl} and ν_{lk} denotes the correlation between the noise power at the kth and lth element of the array,

$$\begin{aligned} \nu_{kl} &= \mathbb{E}\{(n_k^* n_l)\}, \\ \nu_{lk} &= \mathbb{E}\{(n_l^* n_k)\}. \end{aligned} \tag{2.25}$$

The combined noise v_n is minimum when the noise at each element is uncorrelated with noise at the other elements; furthermore, when uncorrelated, the receiver noise consists of only background thermal noise. If an interfering signal emerges, the noise becomes correlated and the combined noise power (v_n) increases, which leads to a decrease in SNR.
Here, s_k is determined based on the direction of the desired incoming signal. For uniform linear arrays, with equally spaced elements s_k is given as:

$$s_k = e^{(i\frac{2\pi kd}{\lambda})\sin\theta}. \tag{2.26}$$

Referring to Figure 2.9 (a), the outputs tend to

$$\begin{aligned} v_s &= \alpha \sum_{k=1}^{K} w_k s_k \\ v_n &= \sum_{k=1}^{K} w_k n_k. \end{aligned} \tag{2.27}$$

The outputs can also be written in matrix notation as:

$$\begin{aligned} v_s &= \alpha \boldsymbol{w}^{\mathrm{T}} \boldsymbol{s} \\ v_n &= \boldsymbol{w}^{\mathrm{T}} \boldsymbol{n}, \end{aligned} \tag{2.28}$$

where $\boldsymbol{w}$, $\boldsymbol{n}$, and $\boldsymbol{s}$ are following vectors respectively: $[w_1, w_2 \ldots w_K]^{\mathrm{T}}$, $[n_1, n_2 \ldots n_K]^{\mathrm{T}}$, $[s_1, s_2 \ldots s_K]^{\mathrm{T}}$.
The output noise power (P_n) is the expected value of the output squared

$$\begin{aligned} P_n &= \mathbb{E}\left\{ |\boldsymbol{v_n}|^{\boldsymbol{2}} \right\} = \mathbb{E}\left\{ \left| \boldsymbol{w}^{\mathrm{T}} \boldsymbol{n} \right|^{\boldsymbol{2}} \right\} \\ &= \mathbb{E}\left\{ \left(\boldsymbol{w}^{\mathrm{T}} \boldsymbol{n} \right)^* \left(\boldsymbol{n}^{\mathrm{T}} \boldsymbol{w} \right) \right\} \\ &= \mathbb{E}\left\{ \boldsymbol{w}^{\mathrm{H}} \boldsymbol{n}^* \boldsymbol{n}^{\mathrm{T}} \boldsymbol{w} \right\}. \end{aligned} \tag{2.29}$$

since, the noise is a random variable, the expectation operator does not effect the weights $\boldsymbol{w}$.

$$\begin{aligned} P_n &= \boldsymbol{w}^{\mathrm{H}} \mathbb{E}\left\{ \boldsymbol{n}^* \boldsymbol{n}^{\mathrm{T}} \right\} \boldsymbol{w} \\ &= \boldsymbol{w}^{\mathrm{H}} \boldsymbol{M} \boldsymbol{w} \\ \text{where } \boldsymbol{M}_{kl} &= \mathbb{E}\left\{ \boldsymbol{n}^* \boldsymbol{n}^{\mathrm{T}} \right\} = [\nu_{kl}]. \end{aligned} \tag{2.30}$$

The covariance matrix ($\boldsymbol{M}$) of the noise components at the antenna elements represents how the noise of the different elements in the array correlate with each other. For instance, when there is no correlation between the antenna elements, the covarience matrix will yield a diagonal matrix as non-diagonal entries shall simply be zero. Since $\nu_{kl} = \nu_{lk}^*$ and $P_n >= 0$ for all $\boldsymbol{w}$, the covariance matrix is by nature a

semi definite hermitian matrix. Thus, because of the nature of the covariance matrix there exists a transformation matrix $\boldsymbol{A}$ capable of diagonalizing the covariance matrix and equalizing the noise power for each element.
With the inclusion of matrix transformation $\boldsymbol{A}$ illustrated in Figure 2.9(b), v_n can be written as:

$$\begin{aligned} v_n &= \hat{\boldsymbol{w}}^{\mathrm{T}}\hat{\boldsymbol{n}} \\ &= \hat{\boldsymbol{w}}^{\mathrm{T}}\boldsymbol{A}\boldsymbol{n}, \end{aligned} \tag{2.31}$$

where the hat symbol signifies that the parameters have already passed through the matrix transform $\boldsymbol{A}$. Similarly, P_n becomes

$$\begin{aligned} P_n &= \mathbb{E}\left\{\left|\hat{\boldsymbol{w}}^{\mathrm{T}}\hat{\boldsymbol{n}}\right|^{\mathbf{2}}\right\} \\ &= \mathbb{E}\left\{\hat{\boldsymbol{w}}^{\mathrm{H}}\hat{\boldsymbol{n}}^{*}\hat{\boldsymbol{n}}^{\mathrm{T}}\hat{\boldsymbol{w}}\right\} \\ &= \hat{\boldsymbol{w}}^{\mathrm{H}}\mathbb{E}\left\{\hat{\boldsymbol{n}}^{*}\hat{\boldsymbol{n}}^{\mathrm{T}}\right\}\hat{\boldsymbol{w}}. \end{aligned} \tag{2.32}$$

There is now an implicit effect caused by the transformation matrix $\boldsymbol{A}$. This implicit effect decorrelates the noise elements and equalizes their powers. Thus,

$$\mathbb{E}\left\{\hat{\boldsymbol{n}}^{*}\hat{\boldsymbol{n}}^{\mathrm{T}}\right\} = \boldsymbol{I}_K, \tag{2.33}$$

which is an identity matrix. P_n then becomes

$$P_n = \hat{\boldsymbol{w}}^{\mathrm{H}}\hat{\boldsymbol{w}} = \|\hat{\boldsymbol{w}}\|^{\mathbf{2}}. \tag{2.34}$$

Since the two block diagrams are equivalent, $v_n = \hat{\boldsymbol{w}}^{\mathrm{T}}\boldsymbol{A}\boldsymbol{n}$ derived in (2.31) is equivalent to $v_n = \boldsymbol{w}^{\mathrm{T}}\boldsymbol{n}$ (2.28) it follows that $\boldsymbol{w} = \boldsymbol{A}^{\mathrm{T}}\hat{\boldsymbol{w}}$ and that (2.30) can then be written as:

$$\begin{aligned} P_n &= \boldsymbol{w}^{\mathrm{H}}\boldsymbol{M}\boldsymbol{w} \\ &= \hat{\boldsymbol{w}}^{\mathrm{H}}\boldsymbol{A}^{*}\boldsymbol{M}\boldsymbol{A}^{\mathrm{T}}\hat{\boldsymbol{w}}. \end{aligned} \tag{2.35}$$

Equating with (2.32), it is easy to observe that

$$\begin{aligned} \boldsymbol{A}^{*}\boldsymbol{M}\boldsymbol{A}^{\mathrm{T}} &= \boldsymbol{I}_K \\ \boldsymbol{M} &= \left(\boldsymbol{A}^{\mathrm{T}}\boldsymbol{A}^{*}\right)^{-1}. \end{aligned} \tag{2.36}$$

Thus, (2.36) now shows explicitly that the transformation matrix $\boldsymbol{A}$ deccorelates and equalizes the covariance matrix $\boldsymbol{M}$. Yet it is not obvious that this indeed maximizes the SNR.
However, with the inclusion of $\boldsymbol{A}$, v_s tends to:

$$\begin{aligned} v_s &= \alpha\hat{\boldsymbol{w}}^{\mathrm{T}}\hat{\boldsymbol{s}} \\ &= \alpha\hat{\boldsymbol{w}}^{\mathrm{T}}\boldsymbol{A}\boldsymbol{s}, \end{aligned} \tag{2.37}$$

by taking the absolute square, and using the Cauchy-Schwarts inequality, the maximum signal power is:

$$|v_s|^2 \leq |\alpha|^2\|\hat{\boldsymbol{w}}\|^2\|\hat{\boldsymbol{s}}\|^2, \tag{2.38}$$

where,

$$\begin{aligned} \|\hat{\boldsymbol{s}}\|^2 &= \hat{\boldsymbol{s}}^{\mathrm{H}}\hat{\boldsymbol{s}} \\ \|\hat{\boldsymbol{w}}\|^2 &= \hat{\boldsymbol{w}}^{\mathrm{H}}\hat{\boldsymbol{w}}. \end{aligned} \tag{2.39}$$

Since $P_n = \|\hat{\boldsymbol{w}}\|^2$, The SNR is:

$$\frac{|v_s|^2}{P_n} \leq |\alpha|^2 \|\hat{\boldsymbol{s}}\|^2. \tag{2.40}$$

Thus, in order to maximize the SNR, the optimal weights $\hat{\boldsymbol{w}}$ should change v_s and P_n such that the equality of (2.40) holds and this occurs when $\hat{\boldsymbol{w}} = \mu\hat{\boldsymbol{s}}^*$, thus substituting $\hat{\boldsymbol{w}} = \mu\hat{\boldsymbol{s}}^*$ into (2.37) and (2.34) yields:

$$\begin{aligned} v_s = \alpha\mu\hat{\boldsymbol{s}}^{\mathrm{H}}\hat{\boldsymbol{s}} = \alpha\mu\|\hat{\boldsymbol{s}}\|^2 \\ P_n = |\mu|^2\|\hat{\boldsymbol{s}}\|^2, \end{aligned} \tag{2.41}$$

and thus the resultant SNR becomes:

$$\frac{|v_s|^2}{P_n} = |\alpha|^2 \|\hat{\boldsymbol{s}}\|^2. \tag{2.42}$$

Which according to (2.40), is the maximum SNR. Thus, indeed proving that the optimal weight $\hat{\boldsymbol{w}} = \mu\hat{\boldsymbol{s}}^*$. Recalling that $\boldsymbol{w} = \boldsymbol{A}^T\hat{\boldsymbol{w}}$ and $\hat{\boldsymbol{s}} = \boldsymbol{A}\boldsymbol{s}$

$$\begin{aligned} \boldsymbol{w}_{\mathbf{opt}} = \boldsymbol{A}^{\boldsymbol{T}}\hat{\boldsymbol{w}}_{\mathbf{opt}} = \boldsymbol{A}^{\boldsymbol{T}}\boldsymbol{\mu}\hat{\boldsymbol{s}}^* \\ \boldsymbol{w}_{\mathbf{opt}} = \mu\boldsymbol{A}^T\boldsymbol{A}^*\boldsymbol{s}^*, \end{aligned} \tag{2.43}$$

which yields $\boldsymbol{w}_{\mathbf{opt}} = \mu\boldsymbol{M}^{-1}\boldsymbol{s}^*$. This can then be re-written as:

$$\boldsymbol{M}\boldsymbol{w} = \mu\boldsymbol{s}^*, \tag{2.44}$$

which is the control law that updates the weight in order to maximize the SNR.

3
Implementation Method

3.1 Simulator

The simulation for this thesis was carried out using a toolbox known as Virmlab which was executed through Matlab. Virmlab is an antenna package that consists of hundreds of objects and functions that are used to simulate various radiation patterns. Virmlab was created by Ulf Carlberg and is a toolbox used frequently at the Gothenburg research center. Due to Virmlab's capability to tweak various antenna parameters and represent corresponding radiation patterns through different plots, it is a suitable candidate to investigate the effectiveness of different beamforming algorithms. Some examples showing the functionality of Virmlab follows.

Figure 3.1 is a 3D representation of the radiated pattern emerging from a 8×1 uniform linear array. The radiation pattern has a main lobe and multiple sidelobes. Having antenna elements along the z-axis, an endfire radiation pattern is produced. From Figure 3.1, it is observed that the radiation pattern is more directive in the mainlobe and less in the sidelobes; although the 3D representation is also a heat map, it is insufficient in quantifying the gain distribution.

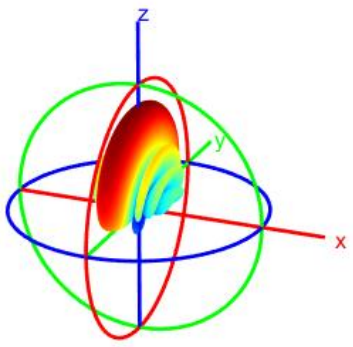

Figure 3.1: 3D plot for broadside array

In order to better quantify the gain distribution, a UV plot is used.

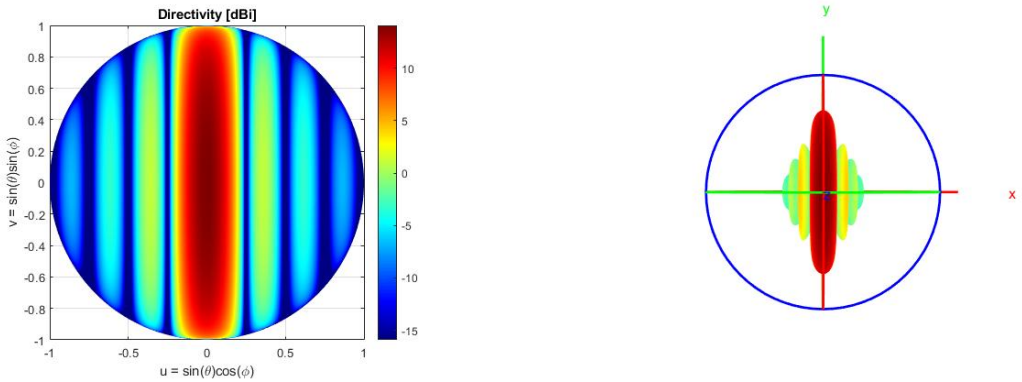

(a) UV plot

(b) 3D representation of UV plot

Figure 3.2: UV plot for broadside array pattern

By applying a conformal mapping and making the transformation $U = \sin(\theta)\cos(\phi)$ and $V = \sin(\theta)\sin(\phi)$, a UV plot is obtained. Figure 3.2(a) is the UV plot for Figure 3.1. It captures Figure 3.1 from a sort of birdlike view, as can be observed in Figure 3.2(b). In essence, the UV plot captures the gain of the radiated pattern in dBi.

Figure 3.3 shows the phasecut plot of Figure 3.1. The phasecut plot zooms in to any angle of the UV plot; thus, it conveys the gain distribution of the UV plot in a more specific manner. Since the phasecut plot captures sidelobes more accurately, it becomes particularly useful when analyzing nulls. Thus, the phasecut plot is used as a sort of interface between the algorithm and its nulling capability.

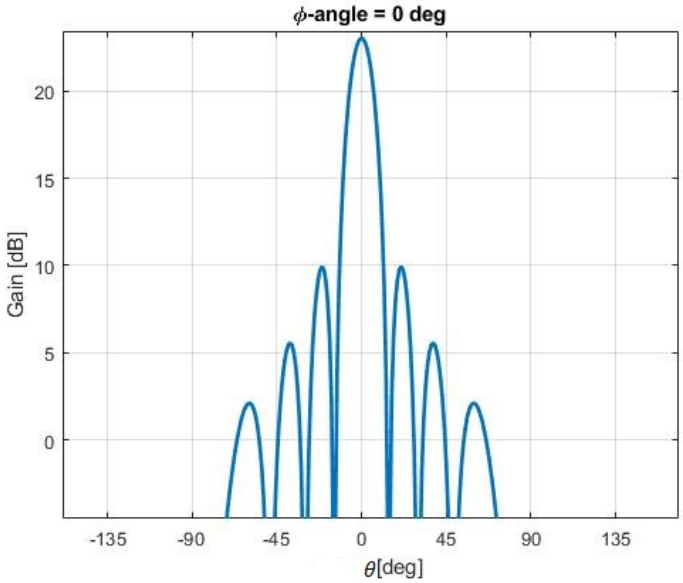

Figure 3.3: Phasecut plot of broadside array pattern

3.2 Simulation scenario

The scenario starts in a quiescent environment, where the only source of noise at the antenna element outputs (P_q) is thermal background noise, which is uncorrelated. Figure 3.4 shows the scenario of a linear uniform array transmitting a desired (blue) signal from base station (BS1) to another uniform linear array located at (BS2); while an undesired (red) jamming signal causes unwanted interference. This interference then becomes a new source of noise for the array at BS2.

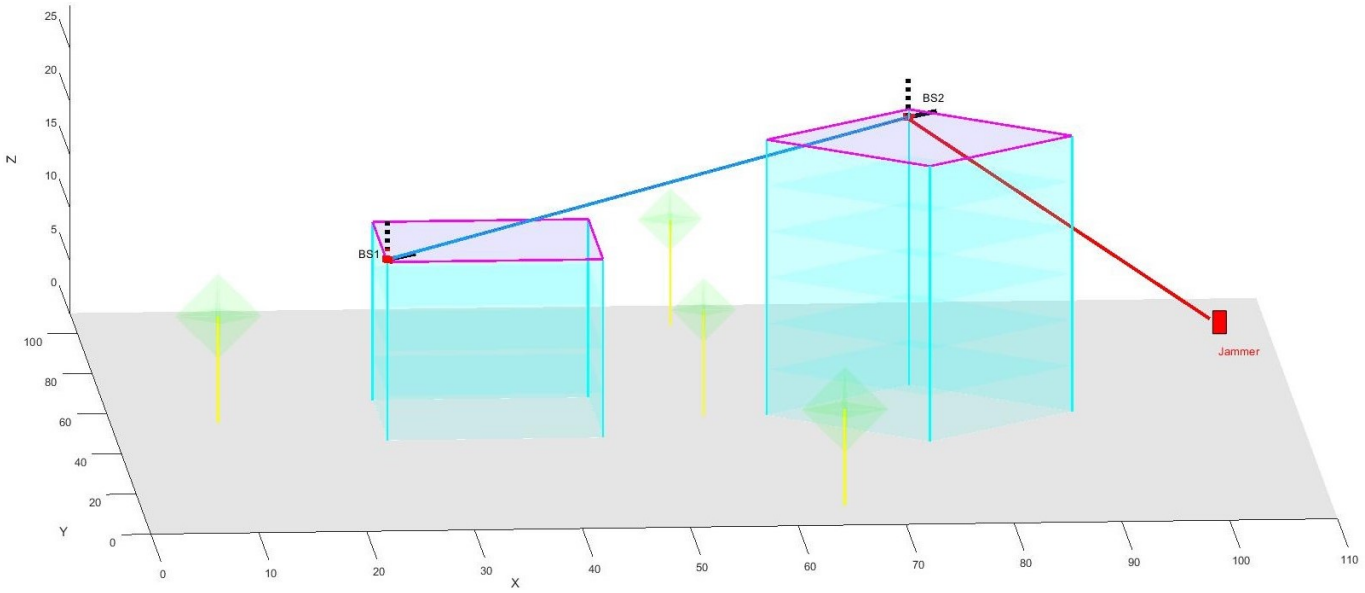

Figure 3.4: A simulated IAB Scenario

The scenario takes place in an xyz coordinate system measured in meters, where BS1 is located at (25, 45, 17) and BS2 at (75, 70, 25). The base stations are placed on top of buildings. The jamming (red) signal is placed arbitrarily; however, it is assumed that the (AoA) and power for the jamming signal is known. This pre-knowledge of whereabouts the jamming signal is coming from can be discovered by using sophisticated algorithms such as the MUSIC algorithm [28]. For the purpose of this thesis, it is assumed that the AoA and jamming power is always known. Although the receiver at the base station knows the direction of the interfering signal; the weights required to suppress the interfering signals are unknown. Thus, by implementing the Applebaum algorithm at the receiver's end, the new weights required to suppress the interference are determined. Figure 3.5(a) shows how the algorithm finds new weights that are needed to suppress an incoming jammer. These new weights comprise of two different set of weights that produce a main array Radiation Pattern Envelope (RPE) and for a cancelling array RPE as shown in Figure 3.5(b).

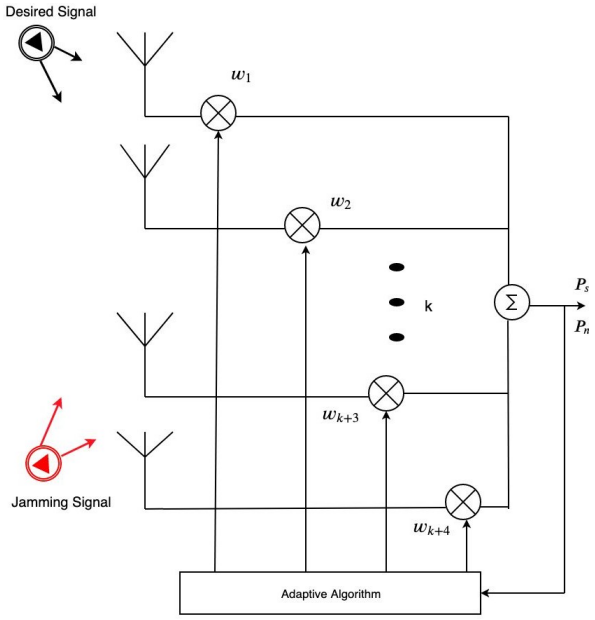

(a) Scenerio for adaptive algorithm

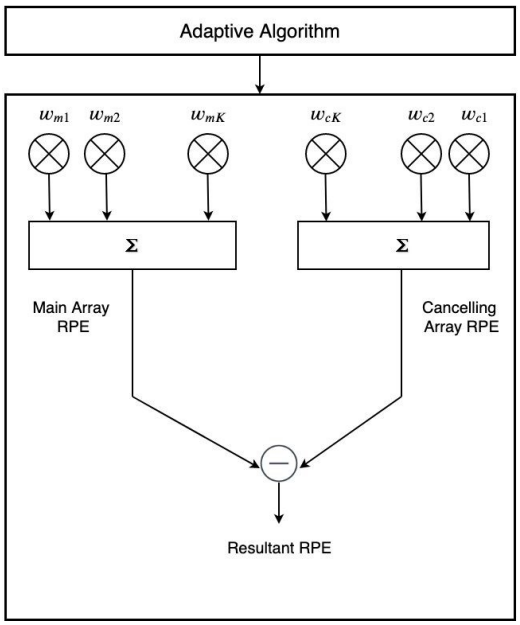

(b) Inside adaptive algorithm

Figure 3.5: Weights applied by the adaptive algorithm

Figure 3.5(b) consists of two different kinds of channels at the subtraction point. The first channel produces a main array RPE, while the second channel produces a cancelling array RPE. The initial weights required to produce the RPE for the main array are known. Through the Applebaum algorithm, new weights estimate a resultant RPE that produces a null at the jammers location. This is better illustrated in Figure 3.6. Figure 3.6 shows an example of applying the Applebaum algorithm on an array which has an RPE that is beamformed at $\theta = 0$ degrees. The initial weights produces this beamformed RPE, which is the main array RPE. Thus, Figure

3.6(a) shows that the jammer's power is initially enhanced by the sidelobe located at approximately 40 degrees.

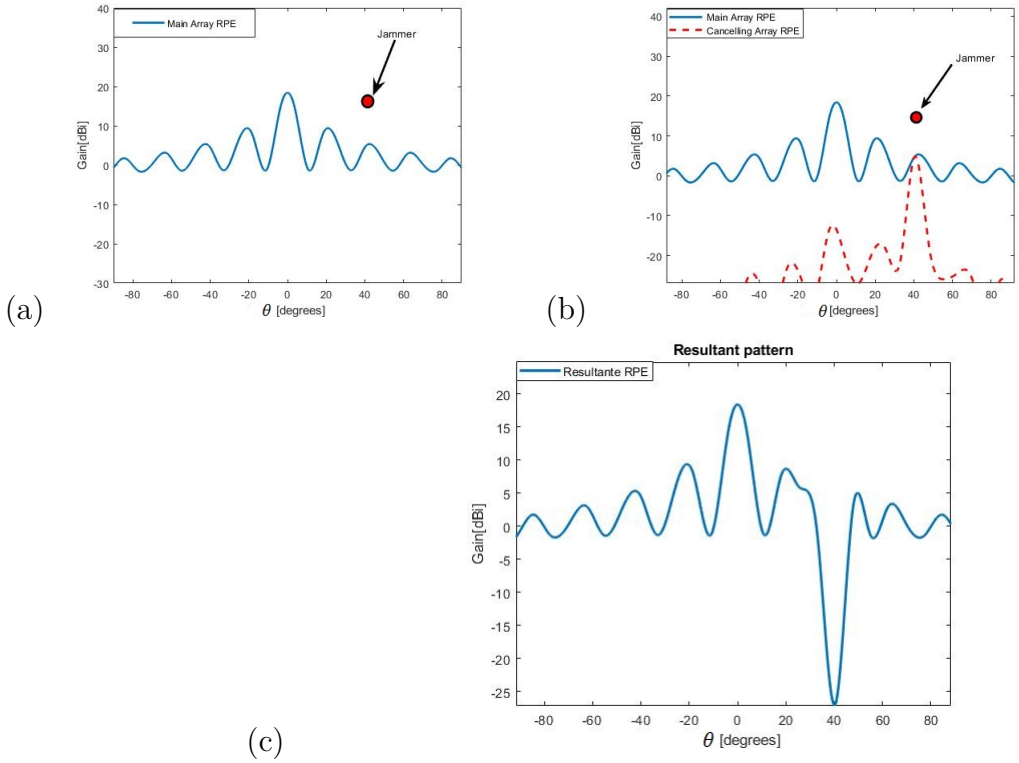

Figure 3.6: Radiation Pattern nulling process

Figure 3.6(b) shows that the cancelling array produces a scaled RPE to estimate the sidelobe location of the jammer. This scaled RPE has a mainlobe which overlaps the sidelobe where the jammer resides. Finally, Figure 3.6(c) shows the resultant RPE produced when the initial weights and cancelling weights are linearly superimposed. The resultant RPE is equivalent to subtracting the main arrays RPE and the cancelling arrays RPE. Thus, due to the null produced, the interference caused by the jamming signal is greatly reduced.
The transmission from BS1 to BS2 is Line of Sight (LoS) and as such, the desired signal follows the Friss transmission equation, where the received power is determined by:

$$\frac{P_r}{P_t} = (\frac{\sqrt{G_t G_r}\lambda}{4\pi r})^2, \tag{3.1}$$

where P_r and P_t stand for the received and transmitted power, G_t and G_r are the gains of the transmitter and receiver, λ is the carrier frequency and r denotes the distance between the transmitter and receiver. Following (3.1) the Equivelent Isotropic Radiated Power (EIRP) is given as:

$$EIRP = P_t \times G_t. \tag{3.2}$$

After alignment, the signal enters through K antenna elements of BS2, where, each antenna element consists of an antenna, a Low Noise Amplifier (LNA) and a phase

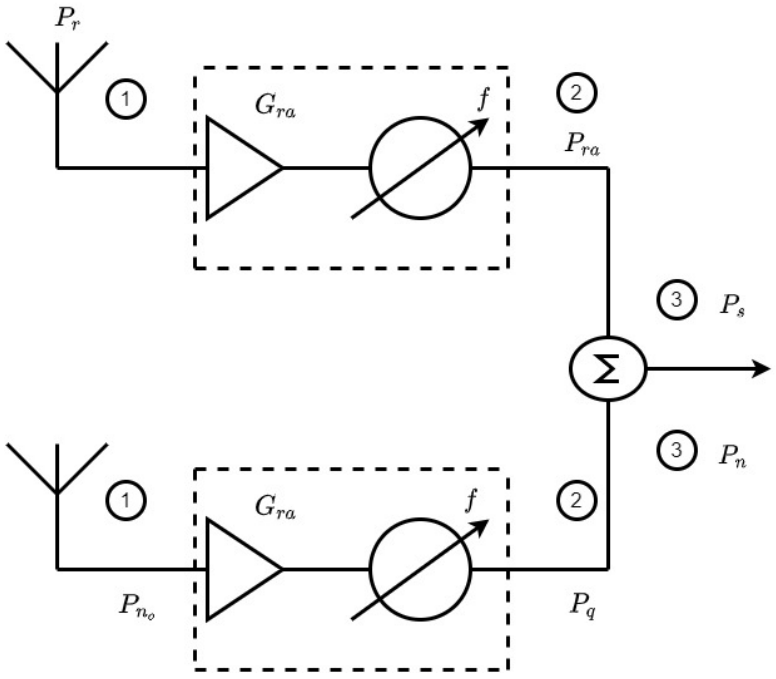

Figure 3.7: Receiver block diagram for SNR calculation

shifter. The signal power (P_s) and the noise power (P_n) is then calculated in 3 stages as shown in Figure 3.7. The upper branch shows the calculation for P_s and the lower branch for P_n. The stages are circled. At stage 1 the received signal power P_r is received following (3.1). Since stage one refers to the very first antenna element, it shall be denoted as P_{r1}. At stage 2, P_{r_1} is multiplied by the LNA gain G_{ra} but, since we are still referring to the the very first element, the LNA gain shall in this case be G_{ra_1}, yielding an output power at the LNA as: $P_{ra} = P_{r1} \times G_{ra1}$. Finally at stage 3, P_{ra} is summed up coherently for K antenna elements; thus, the resultant signal power P_s is: $P_s = \mathrm{K} \times P_{ra}$. P_s can then alternatively be written in dBs as:

$$P_s{}^{dB} = 10 \log_{10}(P_s). \tag{3.3}$$

For the noise calculation it is assumed that the noise power contribution for all antenna elements are identical:
At stage 1, there is only thermal background noise that is denoted as P_{n_0} and given as:

$$P_{n_0} = kT_0B. \tag{3.4}$$

Here k is the Boltzmann constant, T_0 the ambient temperature 290 Kelvins and B the bandwidth. At stage 2, the phase shifter and LNA introduces a gain G_{ra} and a noise figure f; thus the noise power at stage 2 tends to:

$$P_q = G_{ra}fkT_0B. \tag{3.5}$$

At stage 3, the resultant noise power P_n is summed up for K antenna elements: $P_n = \mathrm{K} \times P_q$. Alternatively in dBs:

$$P_n{}^{dB} = 10\log_{10}(P_n). \tag{3.6}$$

The SNR and the SINR can then be calculated as:

$$\begin{aligned} \text{SNR} &= \frac{P_s}{P_n}, \\ \text{SINR} &= \frac{P_s}{P_n + P_I}, \end{aligned} \tag{3.7}$$

respectively, where P_I stands for the power of the jammer which causes interference.

3.3 Applying the Applebaums Algorithm

Recall that (2.36) sets a control law, which adapts antenna element weights so that the SNR of the antenna array is maximized. However, in some applications it is better to have more control on the radiation patterns shape and side lobe levels; furthermore, having the SNR as a governing criteria may limit the use of the algorithm. Instead, it is possible to sacrifice some SNR in order to have better control on the signals radiation pattern [9]. This can be achieved by maximizing on a $\boldsymbol{t}$ vector instead of an $\boldsymbol{s}$ vector, where the $\boldsymbol{t}$ vector is regarded as a generalised signal that has an optimal compromise between gain and sidelobes. Thus, the control law used to update the weights becomes:

$$\boldsymbol{M_q w_q} = \mu \boldsymbol{t}. \tag{3.8}$$

Since the scenario starts in a quiescent environment, there are no jamming signals initially present. As a consequence, the noise component of the antenna elements have equal power and are uncorrelated and thus, the covariance matrix in the quiescent environment is simply a diagonal matrix,

$$\boldsymbol{M_q} = \begin{bmatrix} P_q & & & 0 \\ & P_q & & \\ & & . & \\ & & & . \\ 0 & & & P_q \end{bmatrix}, \tag{3.9}$$

which is equivalent to $P_q \boldsymbol{I}_K$ where, P_q is the noise power, $\boldsymbol{I}_K$ an identity matrix of order K and K, the number of antenna elements. Furthermore, $\boldsymbol{w_q}$ is given as:

$$\boldsymbol{w_q} = \begin{bmatrix} a_1 \\ a_2 e^{-i\beta_s} \\ a_3 e^{-i2\beta_s} \\ . \\ . \\ a_K e^{-i(K-1)\beta_s} \end{bmatrix}, \tag{3.10}$$

where the $a_k s$ are amplitude weights of real numbers and β_s is determined through:

$$\beta_s = \frac{2\pi d}{\lambda}\sin(\theta_s). \tag{3.11}$$

Here, θ_s is the AoA for the desired beamformed signal.
Recall, that $\boldsymbol{M}$ is a covariance matrix for the noise components of antenna elements at the antenna array. Initally $\boldsymbol{M}$ is in a quiescent environment and so $\boldsymbol{M}$ is simply $\boldsymbol{M_q}$ but, when a jammer is introduced, the environment is no longer a quiescent environment and the noise components of the antenna elements are no longer uncorrelated. Furthermore, $\boldsymbol{M}$ changes to $\boldsymbol{M}_q + \boldsymbol{M}_j$, where $\boldsymbol{M}_j$ is the covariance matrix caused by the jammers effect on the noise components of the antenna elements. Thus, new weights are required to adapt to the new noise environment,

$$\begin{aligned} \boldsymbol{Mw} = \boldsymbol{M_q w_q} = P_q \boldsymbol{w_q} \\ \boldsymbol{w} = P_q \boldsymbol{M^{-1} w_q}. \end{aligned} \tag{3.12}$$

If the jammer arrives at an angle θ_j, then due to the uniform linear nature of the array, the jamming signal can be represented at the first element channel as $J(t)$ and at the kth channel as $J(t)e^{-i(k-1)\beta_j}$ where β_j is given as:

$$\beta_j = \frac{2\pi d}{\lambda} \sin(\theta_j). \tag{3.13}$$

Because of this particular representation of the jamming signal within the antenna array, the covariance between the kth and lth element of a covariance matrix $\boldsymbol{M}_j$ with K rows and L columns, where $K = L$, is found to be:

$$\begin{aligned} [\boldsymbol{M}_j]_{k,l} = \mathbb{E}\{(J(t)e^{-i(k-1)\beta_j})(J(t)e^{-i(l-1)\beta_j})^*\} \\ = P_j e^{-i(k-l)\beta_j}. \end{aligned} \tag{3.14}$$

By substituting different rows and columns for k and l in (3.14), the covariance matrix ($\boldsymbol{M}_j$) shall end up having identical values across its diagonals. Thus, $\boldsymbol{M}_j$ is a Hermitian matrix of order K. Being of such nature, it becomes easy to decompose. Thus $\boldsymbol{M}_j$:

$$\boldsymbol{M}_j = P_j \boldsymbol{H^* U H}, \tag{3.15}$$

where P_j represents the average power of the jammer, $\boldsymbol{U}$ is a K $\times$ K matrix of ones and $\boldsymbol{H}$ is:

$$\begin{bmatrix} 1 & 0 & 0 & 0 & 0 \\ 0 & e^{i\beta_j} & 0 & 0 & 0 \\ 0 & 0 & . & 0 & 0 \\ 0 & 0 & 0 & . & 0 \\ 0 & 0 & 0 & 0 & e^{i(\mathrm{K}-1)\beta_j} \end{bmatrix}. \tag{3.16}$$

Thus, by determining β_j and P_j, the covariance matrix due to the jammer is easily obtained. The total covariance matrix is:

$$\begin{aligned} \boldsymbol{M} = \boldsymbol{M}_q + \boldsymbol{M}_j \\ = P_q \boldsymbol{I}_K + P_j \boldsymbol{H^* U H} \end{aligned} \tag{3.17}$$

and thus, $\boldsymbol{M}^{-1}$

$$\boldsymbol{M}^{-1} = \frac{1}{P_q}[\boldsymbol{I}_K - (\frac{P_j}{P_q + KP_j})\boldsymbol{H^* U H}]. \tag{3.18}$$

Substituting into (3.12) the new weights are:

$$\begin{aligned} \boldsymbol{w} &= [\boldsymbol{I_k} - (\frac{P_j}{P_q + KP_j})\boldsymbol{H^* U H}]\boldsymbol{w_q} \\ &= [\boldsymbol{w_q} - (\frac{P_j}{P_q + KP_j})\boldsymbol{H^* U H w_q}]. \end{aligned} \tag{3.19}$$

(3.19) then adapts new weights that enables the algorithm to suppress a jammer provided β_j and P_j are known. (3.19) infers that new weights are produced such that the SNR of the antenna array is maximized with respect to the $\boldsymbol{t}$ vector. It can thus be thought that (3.19) suppresses implicitly. Implicit in the sense that the suppression is achieved through new weights, yet how these new weights influence the radiation pattern remains unknown. Recall though that the last section however illustrates (Figure 3.6) the explicit aspect of suppression on the radiation pattern of the antenna array, and how the algorithm creates a null at a jammers location. This explicit process is derived mathematically by firstly noting that the radiation pattern obtained in the quiescent environment for the weight vector ($\boldsymbol{w}_q$) is a sinc-like function which is expressed as:

$$G_q(\beta) = \sum_{k=1}^{K} a_k e^{j(k-1)(\beta - \beta_s)}, \tag{3.20}$$

where β is the angle of arrival. (3.20) can also be written alternatively as $G_q(\beta) = \boldsymbol{b^T w_q}$ where $\boldsymbol{b^T}$ is given as the transpose of $\boldsymbol{b}$ which is:

$$\boldsymbol{b} = \begin{bmatrix} 1 \\ e^{i\beta} \\ e^{2\beta} \\ . \\ . \\ e^{i(K-1)\beta} \end{bmatrix}. \tag{3.21}$$

Thus, using $G_q(\beta) = \boldsymbol{b^T w_q}$, it is now possible to re-write (3.19) in terms of radiation patterns

$$\boldsymbol{w} = \boldsymbol{w_q} - \frac{P_j}{P_q + KP_j} G_q(\beta_j)\boldsymbol{b}_j^*. \tag{3.22}$$

Multiplying (3.22) by $\boldsymbol{b^T}$ and setting $\boldsymbol{b^T b_j}^* = C(\beta - \beta_j)$, where C is given as: $(e^{i\frac{(K-1)(x)}{2}})(\frac{\sin(Kx/2)}{\sin(x/2)})$. Thus the final radiation pattern is expressed as:

$$G(\beta) = \underbrace{G_q(\beta)}_{\text{Main array RPE}} - \underbrace{\frac{P_j}{P_q + KP_j}}_{\text{Scaling}} \underbrace{G_q(\beta_j)C(\beta - \beta_j)}_{\text{Cancelling RPE}}, \tag{3.23}$$

which shows that the final radiation pattern has a main radiation pattern that is subtracted from a scaled cancelling RPE centered on the jammer.

3.3.1 Applying the Algorithm for Multiple Jammers

A uniform linear array having K elements, has K degrees of freedom in shaping the antenna radiation pattern [7]. Thus, K-1 elements can be used for suppressing interference, while simultaneously maintaining a mainlobe for the desired signal [7]. For multiple jammers, the algorithm is applied in a re-iterative manner, where each iteration counts as a degree of freedom consumed.

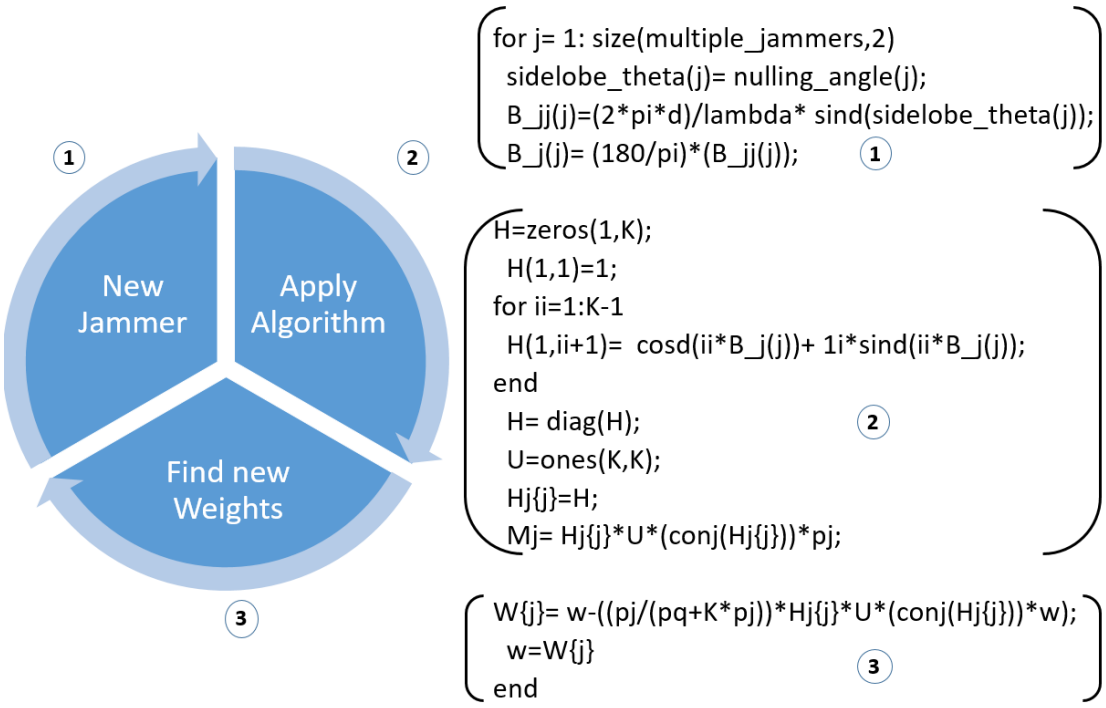

Figure 3.8: The Applebaum algorithm for multiple jammers

Figure 3.8 shows the re-iteration process and its implementation in Matlab. The steps for implementation are indicated by the circled numbers. From the figure we observe that for every jammer (j), one degree of freedom from K is consumed. Thus, K-J yields the number of degrees of freedom that remains, where J is the total number of jammers. Consequently, the number of jammers must always be less then the number of elements in the antenna array ($J < K$).

3.4 Simulation Parameters

The table below summarises the parameters used for the antenna array at the transmitting end, where the ideal array element has a gain (G_t, G_r) of 3.47 dBi.

Element	Type	No. Elements	Elevation (degrees)	Frequency (GHz)	Element Spacing (meters)
Ideal Array Element	Uniform Linear	16	45	27.8	$\frac{\lambda}{2}$

Table 3.1: Transmitting antenna array

The distance (r) between the transmitting array at BS1 and the receiving array at BS2 can be easily calculated to be: $\sqrt{(25-75)^2+(45-25)^2+(17-70)^2} = 75.56$ m. The transmitters power P_t is set to 50 mW per antenna element. The receiving antenna array is also a 16 element array and is assumed to have the same RPE as the transmitting array. The receiving array has an LNA amplifier gain given as $G_{ra} = 20$ dBi. Thus, the receiving antenna array is defined in the table below:

Element	Type	Elevation (degrees)	Element Spacing (meters)	Bandwidth (MHz)	Noise Figure
Ideal Array Element	Uniform Linear	45	$\frac{\lambda}{2}$	400	4

Table 3.2: Recieving antenna array

The simulation is firstly run for the worst case scenario. The jammers power is measured in dBc, which is defined as the ratio between the jamming signal and the desired signal. The jamming signals initial power is set to have approximately the same power as the desired signal. Thus, the initial power for the jammer is set to 0 dBc and then changed later on.
The SNR thresholds required to achieve a certain BER for different modulation schemes are given below as [27]:

BER = 10^{-6}	BPSK	QPSK	16QAM	64QAM
SNR	10.53	13.54	20.42	26.56
n[bits/symbol]	1	2	4	6

Table 3.3: SNR for different modulation formats

4
Results

4.1 Single Jammer

The initial RPE for the transmitting and recieving array has a 3D representation shown in Figure 4.1:

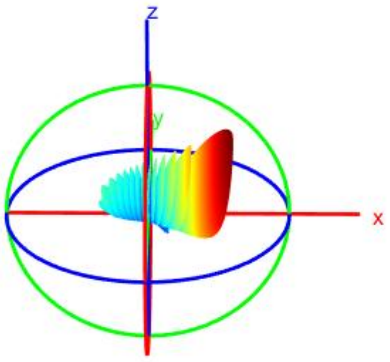

Figure 4.1: 3D Radiation Pattern for transmitting and recieving array

From Figure 4.1, it is observed that the element gain is isotropic along the y-axis and thus the main beam is steered along the x-axis. The corresponding UV plot and phasecut plot are shown in Figure 4.2, which reveals that the mainlobe of the beam is steered at $\theta = 45$ degrees and that the gain of the main lobe is approximately 27.5 dBi. Thus, the EIRP for the transmitting signal is 26.53 dBm. Figure 4.2(b) shows that the largest sidelobe is located left of the mainlobe at an angle of 32 degrees.

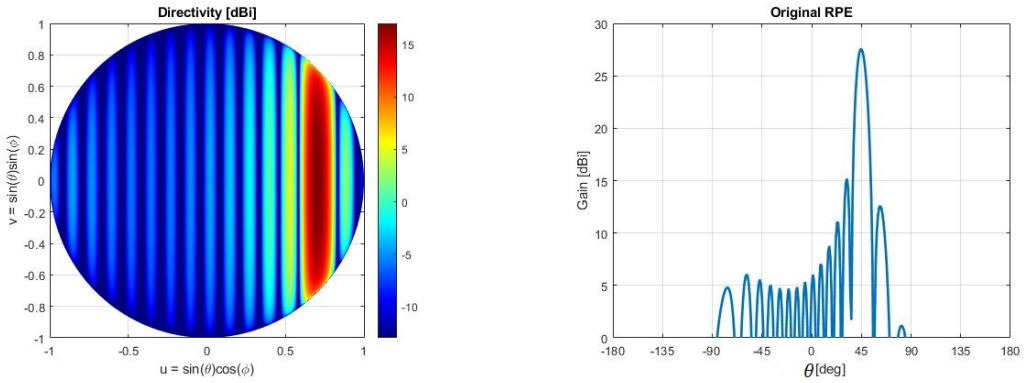

(a) UV (b) Phasecut

Figure 4.2: Transmitting and receiving arrays UV and phascut plot

4.1.1 Quiescent Enviroment

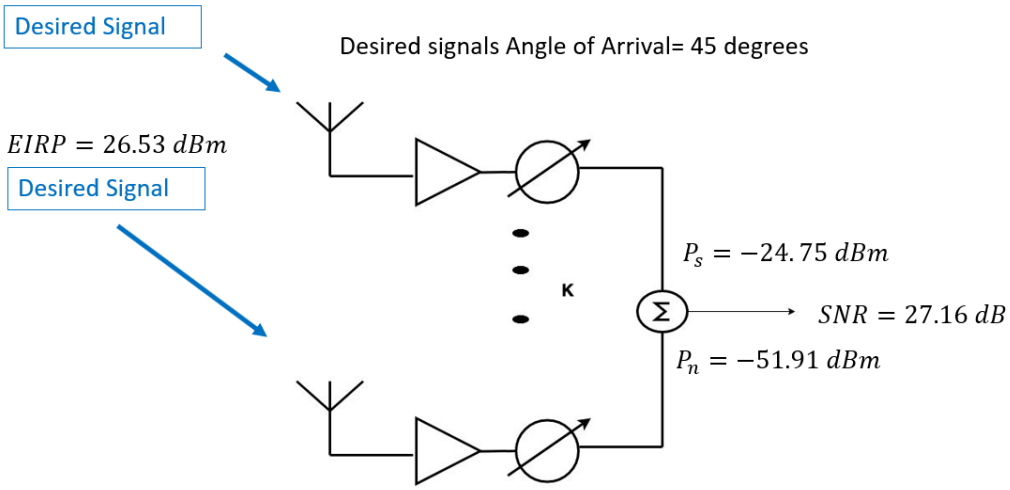

Figure 4.3: Receiver block diagram for quiescent enviroment

With reference to the values given in section 3.4, the signal power, $P_s = -24.75$ dBm and the total noise power of the receiving array is found to be: $P_n = -51.91$ dBm, where each antenna element has a noise power, $P_q = -63.95$ dBm. Thus, in the quiescent environment the SNR is:

$$\text{SNR} = -24.75 - (-51.91) = 27.16 \text{ dB}. \tag{4.1}$$

The covariance matrix in the quiescent environment is shown below as:

$$[\boldsymbol{M}_q]_{1:4,1:4} = \begin{bmatrix} 4.027 \times 10^{-7} & 0 & 0 & 0 \\ 0 & 4.027 \times 10^{-7} & 0 & 0 \\ 0 & 0 & 4.027 \times 10^{-7} & 0 \\ 0 & 0 & 0 & 4.027 \times 10^{-7} \end{bmatrix}.$$

4.1.2 Non-Quiescent Enviroment

Because the sidelobe at 32 degrees is the largest sidelobe, it is then the worst case scenario. Thus, the jammers AoA is initially set at 32 degrees.

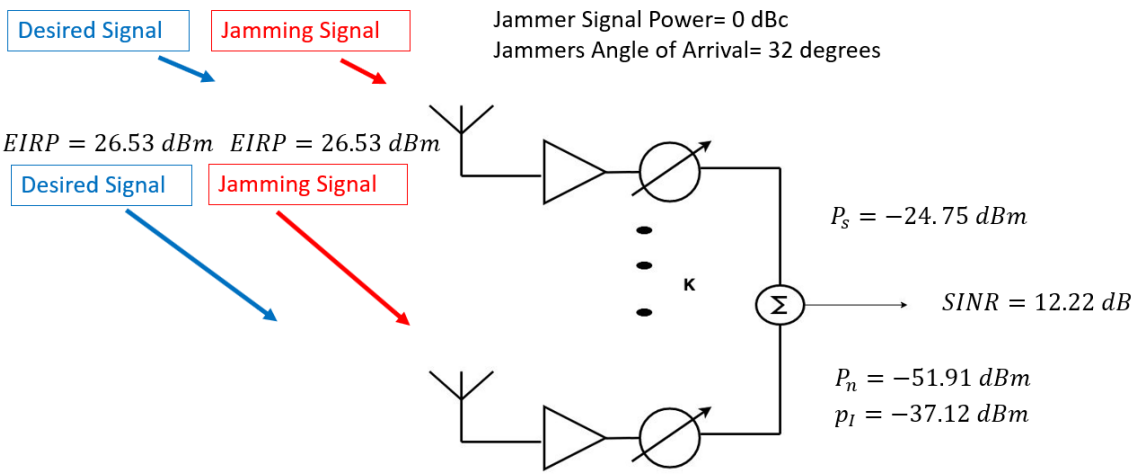

Figure 4.4: Receiver block diagram for non-quiescent enviroment

The jamming signals power is set at 0 dBc with respect to the desired signal. That is to say, the jamming signal has the same EIRP as the desired signal. Thus, P_I tends to -37.12 dBm which causes a SINR of 12.22 dB. A part of the covariance matrix due to the jammer $[\boldsymbol{M}_j]_{1:4,1:4}$ tends to:

$$(10^{-7})\cdot \begin{bmatrix} 7.585+0.000i & -0.712+7.552i & -7.452-1.417i & 2.111-7.286i \\ -0.712-7.552i & 7.586+0.000i & -0.712+7.552i & -7.452-1.417i \\ -7.452+1.417i & -0.712-7.552i & 7.585+0.000i & -0.712+7.552i \\ 2.111+7.286i & -7.452+1.417i & -0.712-7.552i & 7.585+0.000i \end{bmatrix}.$$

4.1.3 Applebaum Algorithm Applied

Using the covariance matrices of the last sections, (3.19) estimates new weights

$$\boldsymbol{w}_{new} = \begin{pmatrix} -0.360 - 0.833i \\ -0.335 + 0.738i \\ 0.728 - 0.283i \\ -0.763 - 0.335i \\ 0.276 + 0.899i \\ 0.630 - 0.853i \\ -1.157 - 0.057i \\ 0.592 + 1.058i \\ 0.592 - 1.058i \\ -1.157 + 0.057i \\ 0.630 + 0.852i \\ 0.276 - 0.899 \\ -0.763 + 0.335i \\ -0.728 + 0.283i \\ -0.335 - 0.738i \\ -0.360 + 0.833i \end{pmatrix}.$$

The resultant radiation pattern produced by the new weights are shown in Figure 4.5:

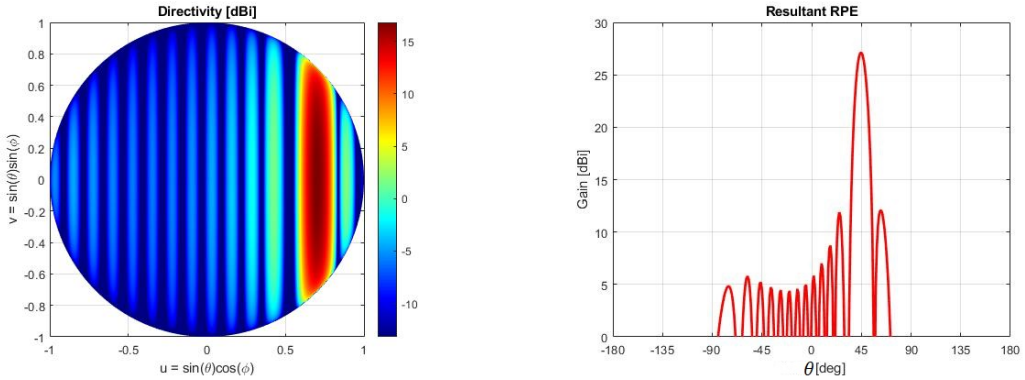

(a) UV plot of resultant RPE

(b) Phasecut plot of Resultant RPE

Figure 4.5: Resultant UV and Phasecut plot after applying the algorithm

In contrast to Figure 4.2, it can be seen that the sidelobe at 32 degrees has been successfully nulled. This can be observed more clearly in the Figure 4.6 below.

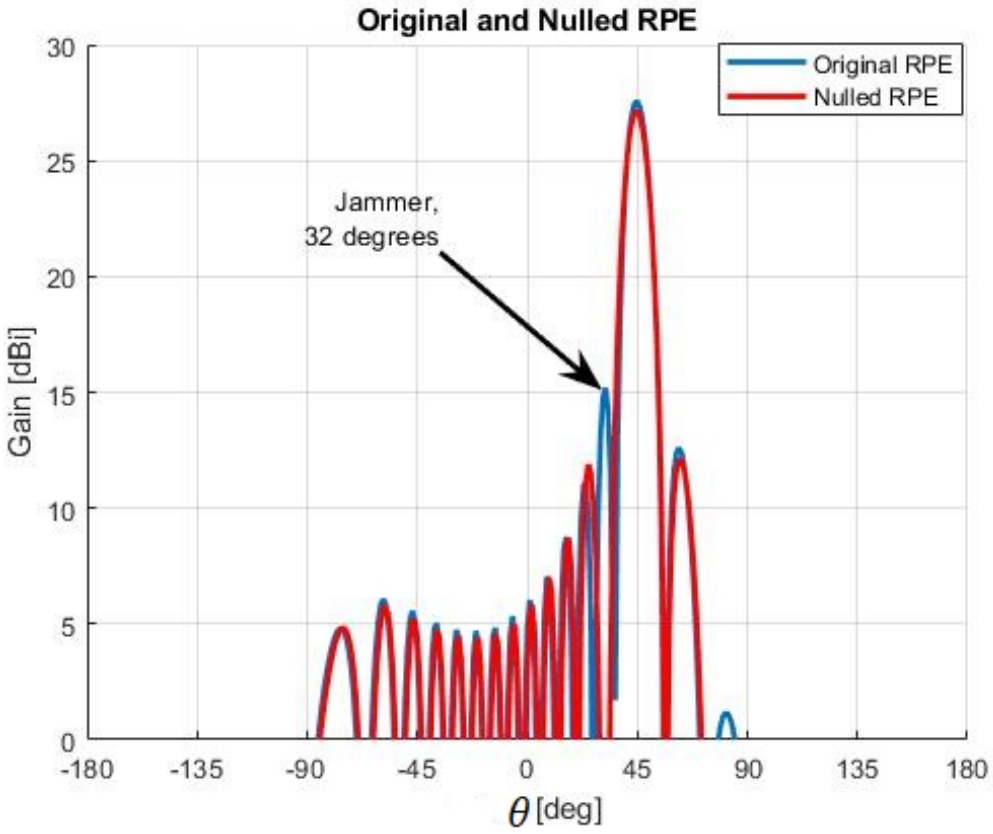

Figure 4.6: Phasecut plot of original and resultant RPE of the receiving array for jammer placed at 32 degrees

Figure 4.6 shows the RPE before and after using the Applebaum algorithm to a jammer placed at 32 degrees. It is observed that the original RPE has slightly higher gain in the mainlobe then the nulled RPE. This then becomes one of the disadvantages of using the algorithm. The algorithm is capable of reducing interference, but it does so at the cost of a slight reduction of the main lobe gain. Figure 4.6 also shows that the nulled RPE has a very similar shape to the original RPE. It can thus be said that the algorithm maintains the shape of the RPE, which is one of the advantages of the algorithm. Figure 4.7 captures the depth of the null produced for the sidelobe located at 32 degrees. The null depth in this report is defined as the change in gain before and after the algorithm is applied.

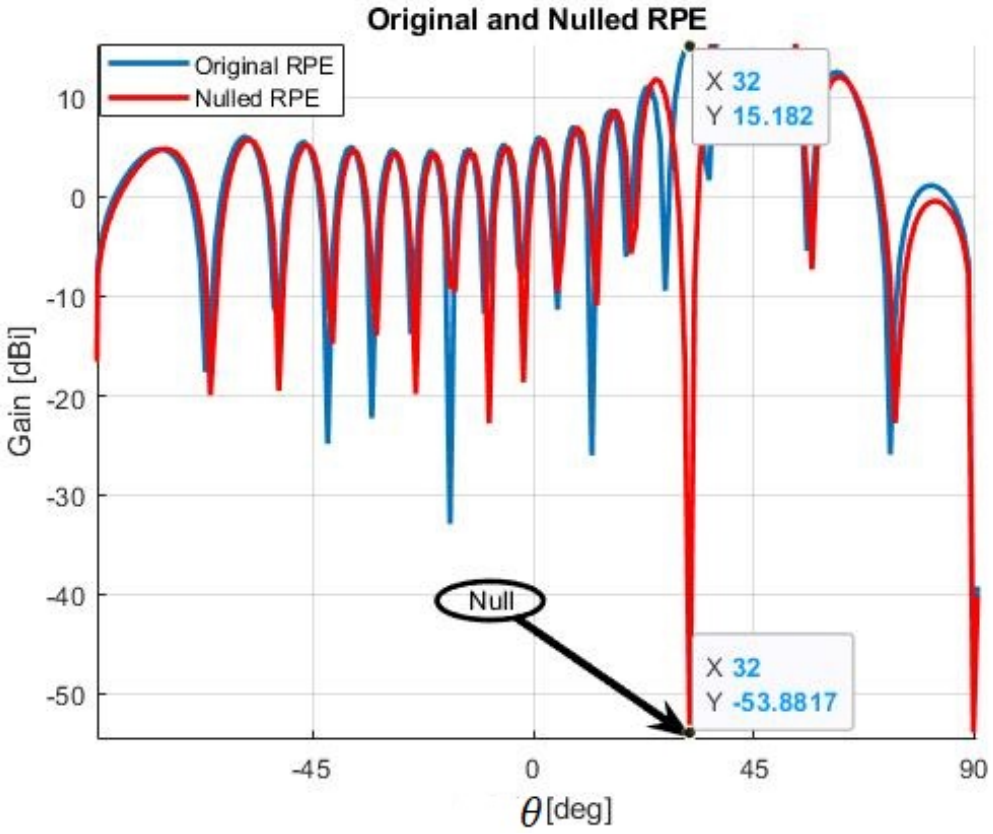

Figure 4.7: Phasecut plot of original and resultant RPE of the receiving array for jammer placed at 32 degrees

The null depth produced at 32 degrees is $15.18 - (-53.88) = 69.06$ dBi. This reduction in gain increases the SINR.

Jamming power(dBc)	SINR_before(dB)	SINR_after(dB)	SINR_improvment(dB)
Pj=-40	27.15	26.73	-0.42
Pj=-20	26.01	26.73	0.72
Pj=0	12.22	26.73	14.51
Pj=20	-7.63	26.73	34.36
Pj=40	-27.63	26.53	54.16

Table 4.1: SINR for different jamming powers

Table 4.1 above conveys what happens when the jamming signal power is assumed to be much lower and higher then the desired signals power. Initially, the jamming power is reduced to -40 dBc, and the SINR improvement is negative. This shows that performing suppression under such an unthreatened condition would result in a loss and not a gain. This is due to the slight reduction in the mainlobe that was eluded to earlier in Figure 4.6. Thus, this would cause a decrease in the signal power term of the SNR, while the noise would remain the same, as the jammers power would be insufficient to affect it.
Table 4.1 also shows what happens as the power of the jammer increases above the

signal power. The SINR after adaptation decreases when the jammer power is 40 dBc. This is to be expected, since regardless of the nulls depth, it shall still have a certain amount of gain. In this case, the gain is approximately -53.88 dBi. Thus, a very powerful jamming signal shall still degrade the system performance even after adaptation. However, it should be noted that the algorithm is able to withstand strong jammers. Even at 40 dBc, the SINR is only 0.03 dB less then the required SNR needed to achieve 64 QAM modulation for a BER of (10^{-6}). If the jamming power increases indefinitely, the improvement in SINR tends to 67.75.

$$\lim_{P_j \to \infty} \text{SINR}_{\text{Improvment}} = 67.75 < 69.06, \tag{4.2}$$

which is less then the null depth. Thus (4.2) shows that the algorithm is lower bounded by the null depth. Furthermore, the higher the null depth, the better the algorithms performance capability.
Table 4.2 below summarises the effect of changing the location of a 0 dBc jammer with respect to the RPE. This change in location will be denoted as the nulling angle in this report.

Elevation(degrees)	45	45	45	45
Nulling angle(degrees)	-29	-6	8	23
SINR Improvment(dB)	11.73	12.29	13.91	17.79

Table 4.2: SINR for jammers with different AoA

The mainlobe for this particular radiation pattern is steered at 45 degrees.

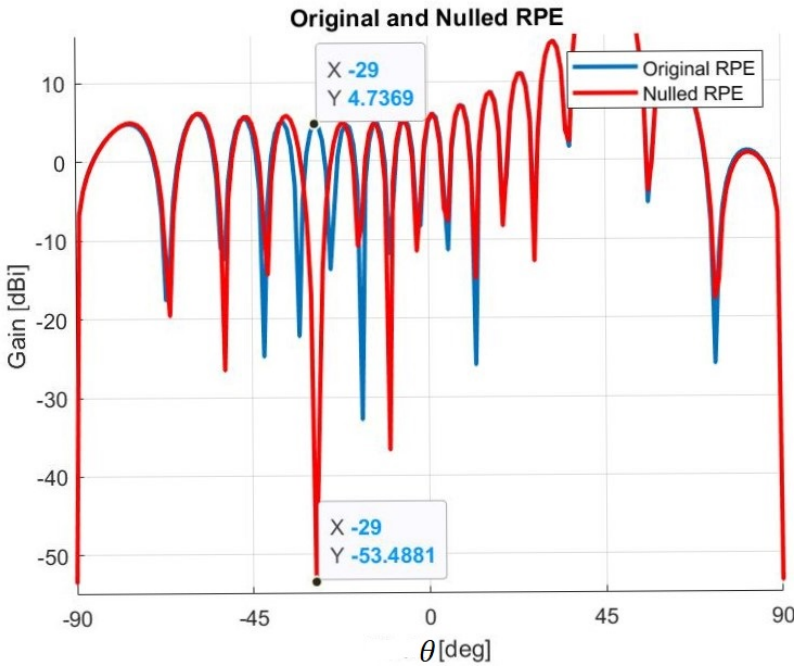

Figure 4.8: Phasecut plot of original and resultant RPE of the receiving array steered at 45 degrees with a jammer placed at -29 degrees

Figure 4.8 shows that the null depth for a jammer placed at -29 degrees tends to: $4.73 - (-53.48) = 58.21$. Table 4.2 shows that as the nulling angle increases, a higher SINR improvement is obtained.

Elevation(degrees)	30	45	60	75
Nulling angle(degrees)	43	16	-26	-13
SINR Improvement(dB)	21.27	15.58	12.31	12.19

Table 4.3: SINR for different array steering angles

In contrast to Table 4.2, Table 4.3 presents what happens when steering the main beam of the array at different elevation angles.

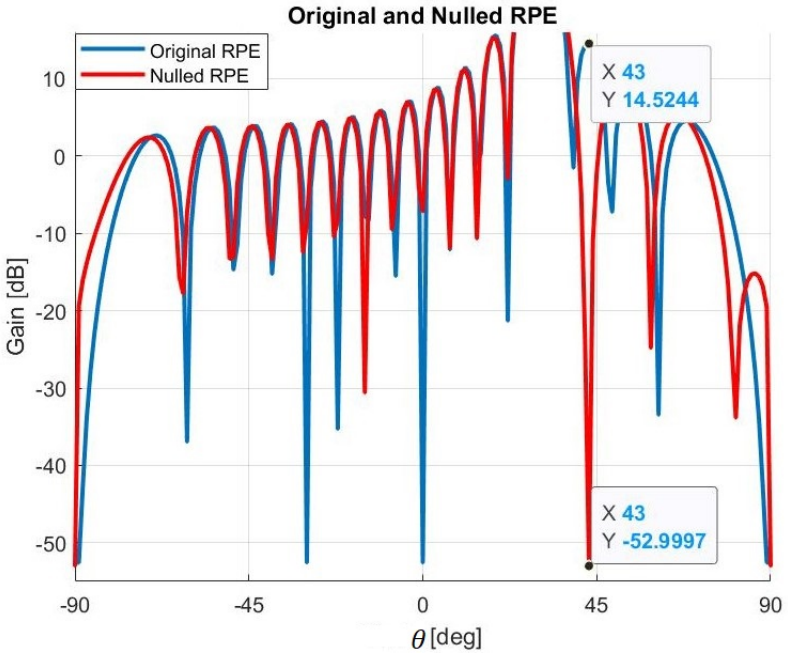

Figure 4.9: Phasecut plot of original and resultant RPE of the receiving array steered at 30 degrees with a jammer placed at 43 degrees

Figure 4.9 captures a null depth of $14.52 - (-52.99) = 68.52$ when the main beam is steered at 30 degrees for a nulling angle at 43 degrees. Comparing Figure 4.9 to 4.8 and the values determined in Table 4.2 and 4.3, it appears that the closer the nulling angle is to the mainlobe the higher the null depth and thus a better improvement in SINR. This is mainly because the sidelobes next to the mainlobe are usually much higher then the sidelobes far from the mainlobe. Thus, the worst case scenario is often found to be when jammers are found near the mainlobe. This does not necessarily mean that it is better to have jammers near the mainlobe, but it does insinuate that the algorithm reaches its full potential when jammers are found near the mainlobe.

4.2 Multiple Jammers

Figure 4.10 and Figure 4.11 show the resulting UV plots obtained after suppression for random multiple jammers in the environment.

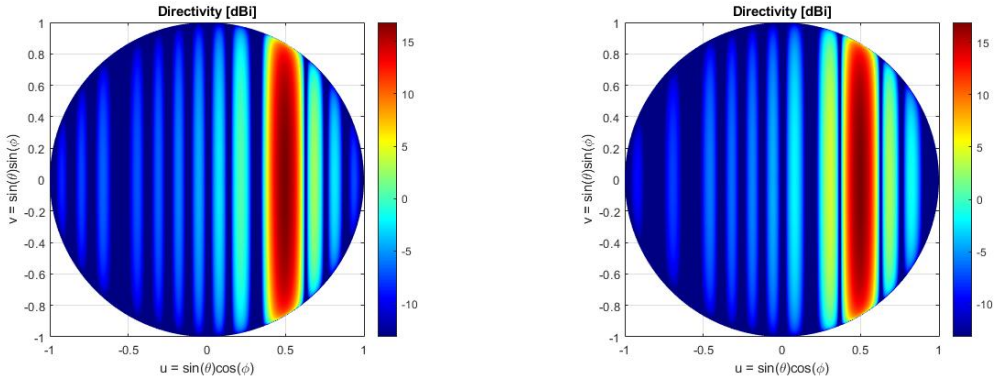

(a) (b)

Figure 4.10: (a)2 jammers (b)4 jammers

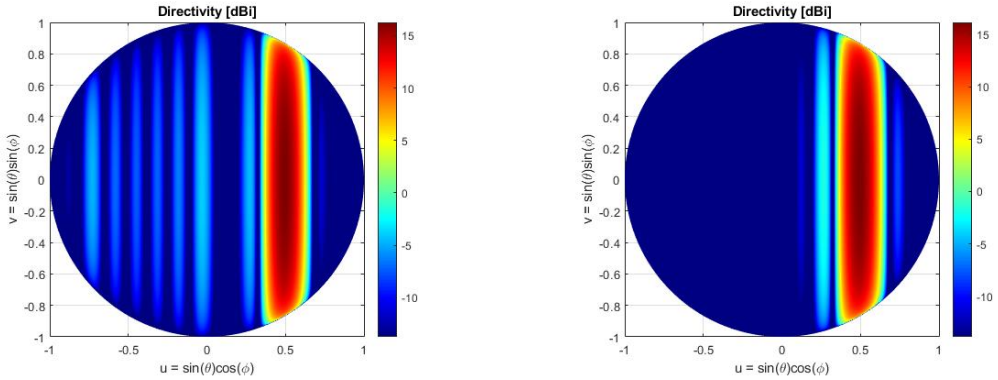

(a) (b)

Figure 4.11: (a)8 jammers (b)15 jammers

Further inspection into the figures suggests that although Figure 4.10(a) and Figure 4.11(a) both suppress the sidelobe to the left of the mainlobe. However, the null produced in Figure 4.11(a) is less than that of Figure 4.10(a). This is also seen when comparing Figure 4.11(a) to 4.11(b). This is because the algorithm is used in a re-iterative manner. The algorithm updates new weights for every new jammer. This is illustrated in Figure 4.12, where 4 jammers are placed on sidelobes located at [-59, -47, 32, 81] degrees and are suppressed sequentially.

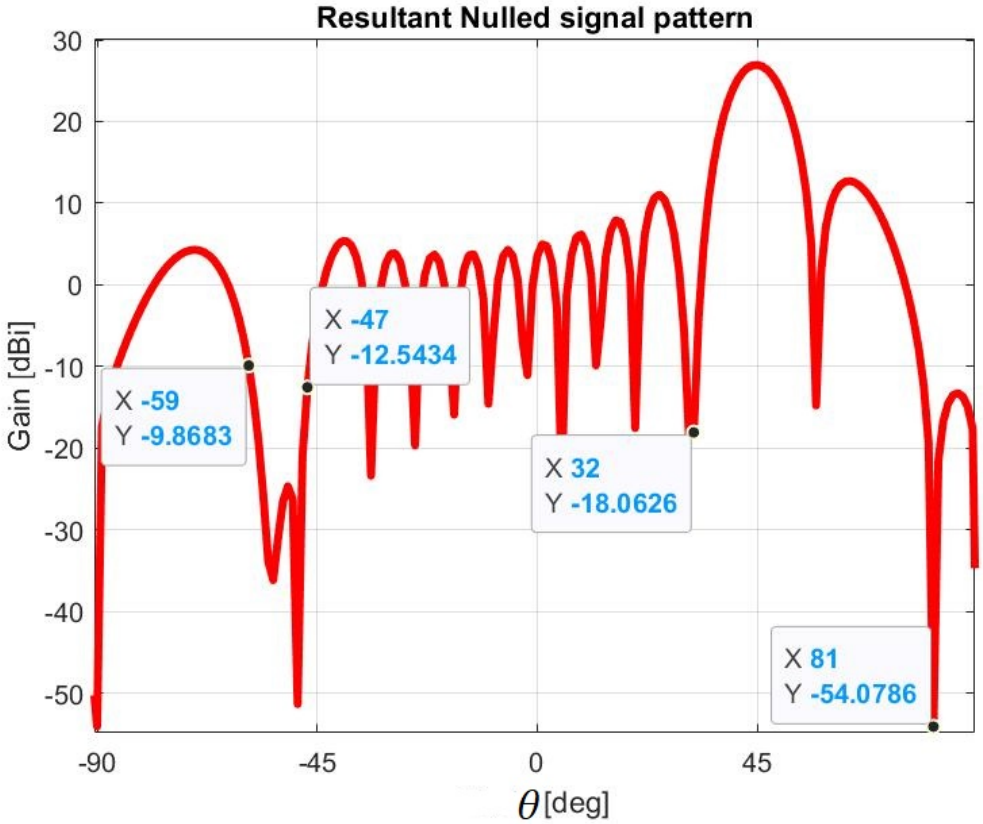

Figure 4.12: Phasecut plot of resultant RPE for receiving array with 4 jammers

Figure 4.12 shows that the nulls produced become weaker as new jammers arrive. Originally a steep null is produced at -59 degrees, but as a new jammer is introduced, a new null must be produced and the old weights are updated accordingly. For every new jammer, the weights move further and further away from the original weights required for the very first jammer at -59 degrees and as a consequence, a weaker null is produced at that particular location. Table 4.4 below shows the effect this has on the SINR improvement.

Elevation(degrees)	45	45	45	45
Number of Jammers	2	4	8	15
Nulling angle(degrees)	-47 32	-59 -47 32 81	-76 -59 -47 -29 8 16 32 81	-76 -59 -47 -37 -29 -21 -13 -6 1 8 16 24 32 81 99
SINR_Before(dB)	11.79	11.21	9.65	7.82
SINR_After(dB)	26.68	26.08	23.74	21.43
SINR_Improvment	14.89	14.87	14.09	13.61

Table 4.4: SINR for multiple jammers with $P_j = 0$ dBc

Table 4.4 consists of jammers placed randomly on different sidelobes, to the left and right of the mainlobe. As the number of jammers increase the SINR improvment decreases. With 4 jammers, the algorithm is only capable of improving the SINR to 26.08 dB which is less than the required SNR needed for 64 QAM modulation format.
How the mainlobe of the RPE changes with the number of jammers is shown in Figure 4.13.

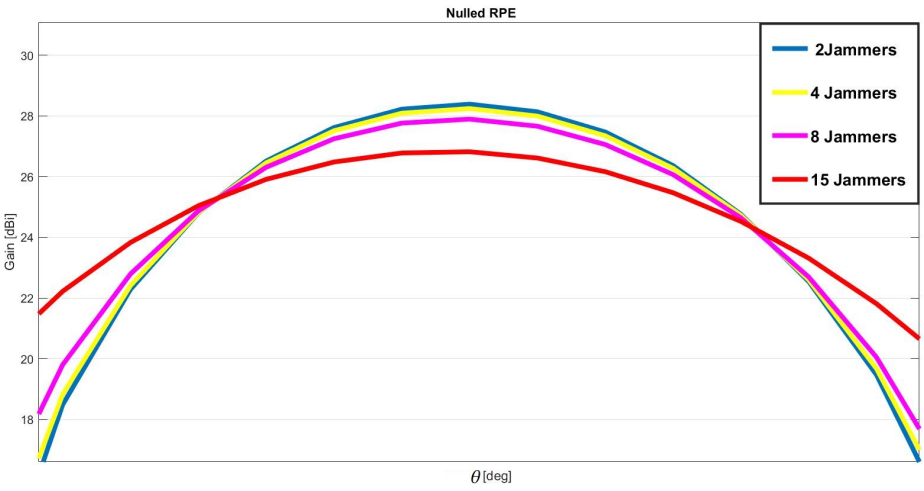

Figure 4.13: Mainlobe for multiple jammers

It is seen from Figure 4.13 that the mainlobe gain decreases with the number of jammers, while the mainlobes width increases. A decrease in gain; results in a lower SINR, and an increase in width shall cause the beam to be less directive. Thus, the algorithms performance is rather limited when it comes to suppressing multiple jammers. Not only does the SINR improvment decrease but the beam also loses its directivity.

4.2.1 Wideband Jammers

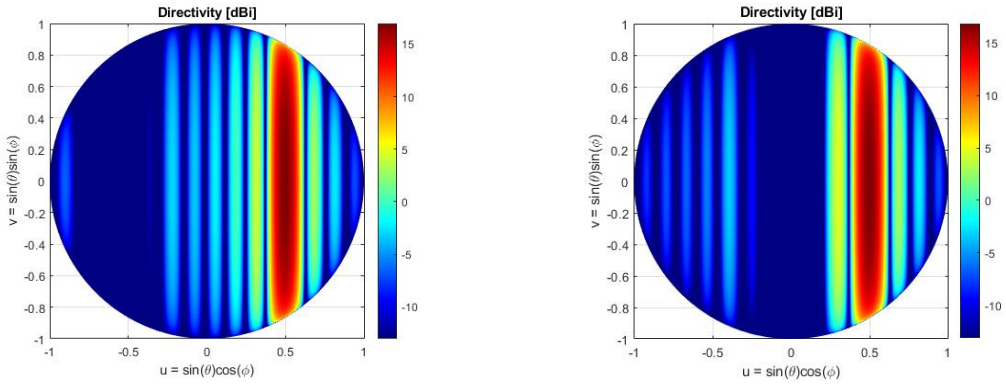

(a) (b)

Figure 4.14: UV plot for Wideband Jammers

Figure 4.14 shows the resulting UV plots for when jammers are assumed to be placed next to each other. The resulting UV plots produce wide nulls and this particular result is especially useful when the jammer is assumed to be wideband in nature. Since a wideband jamming signal encompasses a wider range of angles, the algorithm works particularly well to suppress a wideband jammer by producing nulls for a group of neighbouring sidelobes. If a wideband jamming signal of 800 MHz is transmitted such that is has AoA $\theta = 12$ degrees with a center frequency of 28 GHz (f_0) and a band edge frequency of 28.4 GHz (f), then:

$$\begin{aligned} \Delta \sin(\theta) &= \sin(\theta_0)(1 - \frac{f_0}{f}) \\ &= \sin(12)(1 - \frac{28}{28.4}) = 2.93 \times 10^{-3} \\ \Delta\theta &= \frac{2.93 \times 10^{-3}}{\cos(12)} = 2.99 \times 10^{-3} \text{ rad} = 0.17 \text{ degrees.} \end{aligned} \tag{4.3}$$

Since the jamming signals AoA is 12 degrees, the jammer will cause distortion for 12 ± 0.17 degrees.

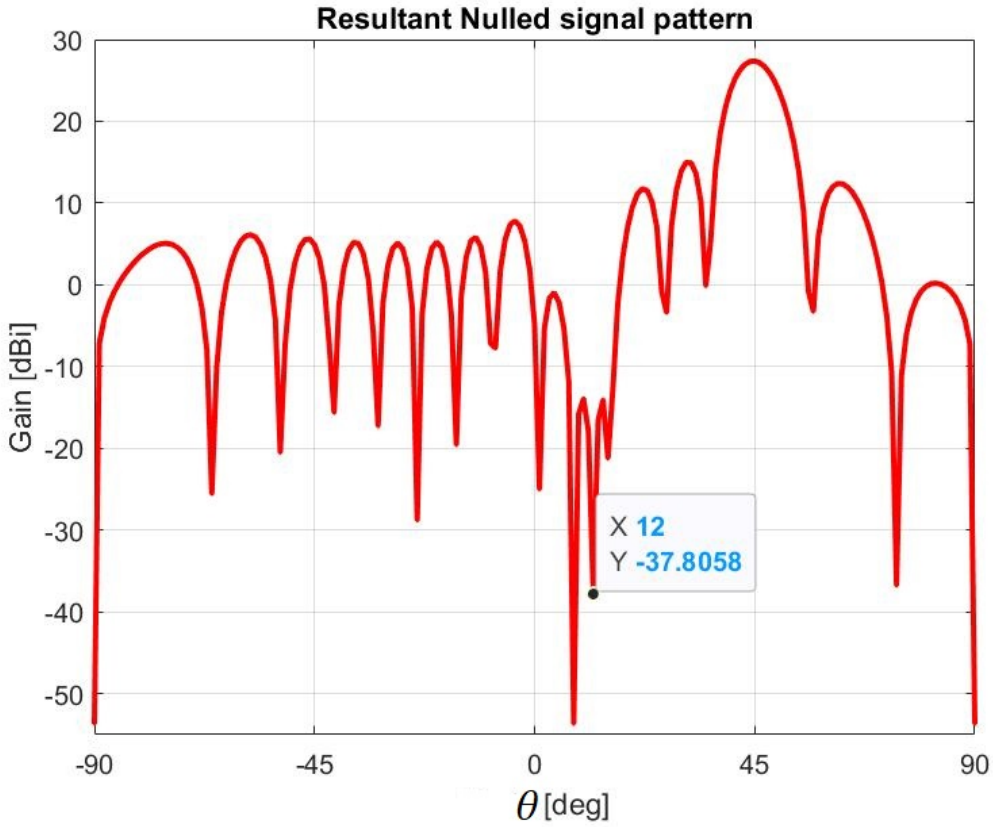

Figure 4.15: Phasecut plot for wideband jammer

Figure 4.15 shows the resultant radiation pattern of producing nulls to the neighbouring sidelobes surrounding 12 degrees. The neighbouring sidelobes closest to 12 degrees include the sidelobes located at 1, 8, 16 degrees. Thus, 3 degrees of freedom were consumed. It can be observed from the Figure 4.15 that the area which 12 ± 0.17 covers has gains that are below -10 dBi.

5
Conclusion

Integrating access and backhaul in 5G has its trade-offs. On one hand, it saves costs and allows for easier deployment of base stations, on the other hand, there is an increased probability of interference. Applying the Applebaum algorithm in the context of an IAB scenario not only results in interference suppression but also addresses the near-far problem by taking into account the power of the jamming signal.
Simulations were run to test the upper and lower limits of the Applebaum algorithm. It was found that the algorithm can improve system performance by suppressing jammers up to 40 dBc while also maintaining the radiation pattern shape of the receiving antenna array.
By updating the weights in an iterative manner it was shown that the algorithm could also be used to suppress multiple jammers but, this is to be at the expense of consuming a degree of freedom for every new jammer. Furthermore, it was revealed that when suppressing multiple jammers not all the nulls produced are as deep and as a result, the capability of the algorithm in improving system performance for multiple jammers is more limited. The algorithm could not accommodate more then 3 jammers without compromising the system performance. However, this turned out to be enough degrees of freedom needed to suppress a wideband signal of 800 MHz.

Bibliography

[1] P. Tripathi and R. Prasad, "Spectrum for 5G Services", Wireless Personal Communications, vol. 100, no. 2, pp. 539-555, 2018.

[2] M. Islam, S. Subramanian and A. Sampath, "Integrated Access Backhaul in Millimeter Wave Networks", 2017 IEEE Wireless Communications and Networking Conference (WCNC), 2017. Available: 10.1109/wcnc.2017.7925837 [Accessed 11 February 2019].

[3] 3GPP TR 38.874, 3rd generation partnership project: technical specification Group Radio Access Network; NR;Study on Integrated Access and Backhaul; (release 16), V16.0.0, 2018.

[4] "Antenna Array Basics", Antenna Arrays, pp. 1-44, 2010.

[5] J. Grubor, V. Jungnickel and K. Langer, "Rate-adaptive multiple sub-carrier-based transmission for broadband infrared wireless communication", Optical Fiber Communication Conference and the National Fiber Optic Engineers Conference, 2006.

[6] F. Huang, W. Sheng and X. Ma, "Modified projection approach for robust adaptive array beamforming", Signal Processing, vol. 92, no. 7, pp. 1758-1763, 2012.

[7] A. Fenn, *Adaptive antennas and phased arrays for radar and communications* Boston: Artech House, 2008.

[8] Ali, E., Ismail, M., Nordin, R. and Abdulah, N., 2017. Beamforming techniques for massive MIMO systems in 5G: overview, classification, and trends for future research. *Frontiers of Information Technology Electronic Engineering*, 18(6), pp.753-772.

[9] Applebaum, S. and Chapman, D. (1976). Adaptive arrays with main beam constraints. *IEEE Transactions on Antennas and Propagation*, 24(5), pp.650-662.

[10] A. Erokhin, E. Gafarov and P. Shtro, "A Method of Equalizing Frequency Responses of Adaptive Antenna Array Channels", 2019.

[11] W. Stutzman and G. Thiele, *Antenna theory and design* Hoboken, NJ: Wiley, 2013.

[12] C. Balanis, *Modern Antenna Handbook.* Somerset: Wiley, 2011.

[13] S. Bhuiya, F. Islam and M. Matin, "Analysis of Direction of Arrival Techniques Using Uniform Linear Array",*International Journal of Computer Theory and Engineering*, pp. 931-934, 2012.

[14] Q. Shen, W. Liu, W. Cui, S. Wu, Y. Zhang and M. Amin, "Wideband DOA estimation for uniform linear arrays based on the co-array concept",2015 23rd European Signal Processing Conference (EUSIPCO), 2015.

[15] S. K. Garakoui, E. A. M. Klumperink, B. Nauta and F. E. van Vliet, "Phased-array antenna beam squinting related to frequency dependency of delay circuits," 2011 41st European Microwave Conference, Manchester, 2011, pp. 1304-1307, doi: 10.23919/EuMC.2011.6101846.

[16] A. Zaidi, F. Athley, J. Medbo, U. Gustavsson, G. Durisi and X. Chen, *5G physical layer*. London: Academic Press, 2018.

[17] E. Dahlman et al., "5G wireless access: requirements and realization", *IEEE Communications Magazine*, vol. 52, no. 12, pp. 42-47, 2014. Available: 10.1109/mcom.2014.6979985.

[18] C. Saha, M. Afshang and H. Dhillon, "Bandwidth Partitioning and Downlink Analysis in Millimeter Wave Integrated Access and Backhaul for 5G", *IEEE Transactions on Wireless Communications*, vol. 17, no. 12, pp. 8195-8210, 2018. Available: 10.1109/twc.2018.2874655.

[19] T. Rappaport, *Wireless communicators*. Upper Saddle River, N.J.: Prentice Hall PTR, 2002.

[20] 3GPP TS 38.101-1, NR; User Equipment (UE) radio transmission and reception; Part 1: Range 1 Standalone, 2017.

[21] Ngo, "Massive MIMO: Fundamentals and System Designs", PH.D, Linköping University, 2015.

[22] M. Costa, "Writing on dirty paper (Corresp.)", *IEEE Transactions on Information Theory*, vol. 29, no. 3, pp. 439-441, 1983.

[23] X. Gao, O. Edfors, F. Rusek and F. Tufvesson, "Linear Pre-Coding Performance in Measured Very-Large MIMO Channels", *2011 IEEE Vehicular Technology Conference (VTC Fall)*, 2011. Available: 10.1109/vetecf.2011.6093291 [Accessed 24 July 2019].

[24] N. Fatema, G. Hua, Y. Xiang, D. Peng and I. Natgunanathan, "Massive MIMO Linear Precoding: A Survey", *IEEE Systems Journal*, vol. 12, no. 4, pp. 3920-3931, 2018.

[25] H. Singh and R. Jha, "Trends in Adaptive Array Processing", *International Journal of Antennas and Propagation*, vol. 2012, pp. 1-20, 2012.

[26] M. Al-Sadoon, R. Abd-Alhameed and I. Elfergani, "Weight Optimization for Adaptive Antenna Arrays Using LMS and SMI Algorithms", WSEAS TRANSACTIONS on COMMUNICATIONS, vol. 15, 2016.

[27] J. Grubor, V. Jungnickel and K. Langer, "Rate-adaptive multiple sub-carrier-based transmission for broadband infrared wireless communication", 2006 Optical Fiber Communication Conference and the National Fiber Optic Engineers Conference, 2006. Available: 10.1109/ofc.2006.215924 [Accessed 16 August 2019].

[28] X. Cao, H. Liu and S. Wu, "DOA Estimation Based on Online Music Algorithm", Journal of Electronics Information Technology, vol. 30, no. 11, pp. 2658-2661, 2011.